

New PARSEC database of α -enhanced stellar evolutionary tracks and isochrones I. Calibration with 47 Tuc (NGC104) and the improvement on RGB bump

Xiaoting Fu¹, Alessandro Bressan¹, Paola Marigo², Léo Girardi³, Josefina Montalbán², Yang Chen², Ambra Nanni²

¹ SISSA - International School for Advanced Studies, via Bonomea 265, 34136 Trieste, Italy

² Dipartimento di Fisica e Astronomia Galileo Galilei, Università di Padova, Vicolo dell'Osservatorio 3, I-35122 Padova, Italy

³ INAF - Osservatorio Astronomico di Padova, Vicolo dell'Osservatorio 5, I-35122 Padova, Italy

23 January 2018

ABSTRACT

Precise studies on the Galactic bulge, globular cluster, Galactic halo and Galactic thick disk require stellar models with α enhancement and various values of helium content. These models are also important for extra-Galactic population synthesis studies. For this purpose we complement the existing PARSEC models, which are based on the solar partition of heavy elements, with α -enhanced partitions. We collect detailed measurements on the metal mixture and helium abundance for the two populations of 47 Tuc (NGC 104) from the literature, and calculate stellar tracks and isochrones with these α -enhanced compositions. By fitting the precise color-magnitude diagram with *HST ACS/WFC* data, from low main sequence till horizontal branch, we calibrate some free parameters that are important for the evolution of low mass stars like the mixing at the bottom of the convective envelope. This new calibration significantly improves the prediction of the RGB bump brightness. Comparison with the observed RGB and HB luminosity functions also shows that the evolutionary lifetimes are correctly predicted. As a further result of this calibration process, we derive the age, distance modulus, reddening, and the red giant branch mass loss for 47 Tuc. We apply the new calibration and α -enhanced mixtures of the two 47 Tuc populations ($[\alpha/\text{Fe}] \sim 0.4$ and 0.2) to other metallicities. The new models reproduce the RGB bump observations much better than previous models. This new PARSEC database, with the newly updated α -enhanced stellar evolutionary tracks and isochrones, will also be part of the new stellar products for *Gaia*.

Key words: stars: evolution, stars: Hertzsprung-Russell diagram, stars: colour-magnitude diagrams; stars: low-mass, stars: interiors

1 INTRODUCTION

PARSEC (PAдова-TRieste Stellar Evolution Code) is widely used in the astronomical community. It provides input for population synthesis models to study resolved and unresolved star clusters and galaxies (e.g. Perren, Vázquez & Piatti 2015; Gutkin, Charlot & Bruzual 2016; Chevillard & Charlot 2016), and offers reliable models for many other field of studies, such as to derive black hole mass when observing gravitational waves (e.g. Spera, Mapelli & Bressan 2015; Belczynski et al. 2016), to get host star parameters for exoplanets (Santos et al. 2013; Maldonado et al. 2015, etc.), to explore the mysterious “cosmological lithium problem” (Fu et al. 2015), to derive the main parameters of star clusters (for instance, Donati et al. 2014; Borissova et al. 2014; San Roman et al. 2015; Goudfrooij et al. 2015) and Galactic structure (e.g. Küpper et al. 2015; Li et al. 2016; Balbinot et al. 2016; Ramya et al. 2016), to study dust formation (e.g. Nanni et al.

2013; Nanni et al. 2014), to constrain dust extinction (e.g. Schlafly et al. 2014; Schultheis et al. 2015; Bovy et al. 2016), and to understand the stars themselves (e.g. Kalari et al. 2014; Smiljanic et al. 2016; Gullikson, Kraus & Dodson-Robinson 2016; Reddy & Lambert 2016; Casey et al. 2016), etc.

There are now four versions of PARSEC isochrones available online¹. The very first version PARSEC v1.0 (Bressan et al. 2012) provides isochrones for $0.0005 \leq Z \leq 0.07$ ($-1.5 \leq [M/H] \leq +0.6$) with the mass range $0.1 M_{\odot} \leq M < 12 M_{\odot}$ from pre-main sequence to the thermally pulsing asymptotic giant branch (TP-AGB). In PARSEC v1.1 (based on Bressan et al. 2012) we expanded the metallicity range down to $Z=0.0001$ ($[M/H]=-2.2$). PARSEC v1.2S included big improvements both on the very low mass stars and massive stars: Chen et al. (2014) improve the sur-

¹ CMD input form: <http://stev.oapd.inaf.it/cgi-bin/cmd/>

face boundary conditions for stars with mass $M \lesssim 0.5 M_{\odot}$ in order to fit the mass-radius relation of dwarf stars; Tang et al. (2014) introduce mass loss for massive star $M \geq 14 M_{\odot}$; Chen et al. (2015) improve the mass-loss rate when the luminosity approaches the Eddington luminosity and supplement the model with new bolometric corrections till $M=350 M_{\odot}$. In a later version (PARSEC v1.2S + COLIBRI PR16) we describe improved isochrones with the addition of COLIBRI (Marigo et al. 2013) evolutionary tracks of TP-AGB stars (Rosenfield et al. 2016; Marigo et al. 2017).

All previous versions of PARSEC models are calculated assuming solar-scaled metal mixtures, in which the initial partition of heavy elements keeps always the same relative number density as that in the Sun. It is now well established that the solar-scaled metal mixture is not universally applicable for all types of stars. In fact, one of the most important group of elements, the so called α -elements group, is not always observed in solar proportions. Many studies have confirmed the existence of an “enhancement” of α -elements in the Milky Way halo (e.g. Zhao & Magain 1990; Nissen et al. 1994; McWilliam et al. 1995; Venn et al. 2004), globular clusters (e.g. Carney 1996; Sneden 2004; Pritzl, Venn & Irwin 2005), the Galactic Bulge (Gonzalez et al. 2011; Johnson et al. 2014), and thick disk (e.g. Fulbright 2002; Reddy, Lambert & Prieto 2006; Ruchti et al. 2010). Stars in the dwarf spheroidal Milky Way satellite galaxies show different α -abundance trends compared to the Galactic halo stars, possibly indicating different star formation paths (Kirby et al. 2011). The α -elements (O, Ne, Mg, Si, S, Ar, Ca, and Ti) are mainly produced by core collapse (mostly Type II) supernovae (SNe) on short timescale, while the iron-peak elements (V, Cr, Mn, Fe, Co and Ni) are mainly synthesized in Type Ia SNe on longer timescales. Therefore, the evolution profile of $[\alpha/\text{Fe}]$ records the imprint of the star formation history of the system. An alternative explanation could be that the Initial Mass Function (IMF) of the α -enhanced stellar populations was much richer in massive stars than the one from which our Sun was born (Chiosi et al. 1998). However there is no clear evidence in support of this alternative possibility.

In order to model star clusters, galaxies and Galactic components more precisely, the previous Padova isochrone database offered a few sets of α -enhanced models for four relatively high metallicities (Salasnich et al. 2000), other stellar evolution groups also published isochrones that allow for α enhancement (e.g. VandenBerg et al. 2000, 2014; Pietrinferni et al. 2006; Valcarce, Catelan & Sweigart 2012). Now, with the thorough revision and update input physics, we introduce α -enhanced metal mixtures in PARSEC.

In this paper we first calibrate the new PARSEC α -enhanced stellar evolutionary tracks and isochrones with the well-studied globular cluster 47 Tucanae (NGC 104). Then we apply the calibrated parameters to obtain models for other metallicities. Section 2 briefly describes the input physics. Section 3 introduces the comparison with 47 Tuc data in details, including the isochrone fitting and luminosity function, envelope overshooting calibration with red giant branch bump, and mass loss in the red giant branch (RGB) from horizontal branch (HB) morphology. Section 4 compares the new PARSEC models with other stellar models and shows its improvement on RGB bump prediction. A summary of this paper and the discussion are in Section 5.

2 INPUT PHYSICS

The main difference with respect to the previous versions of PARSEC is the adoption of new nuclear reaction rates, α -enhanced opacities, and various helium contents.

We update the nuclear reaction rates from JINA REACLIB database (Cyburt et al. 2010) with their April 6, 2015 new recommendation. In addition, more reactions – 52 instead of the 47 described in Bressan et al. (2012) for the previous versions of PARSEC – are taken into account. They are all listed in Table 1 together with the reference from which we take the reaction energy Q value. In the updated reactions, more isotopic abundances are considered, in total $N_{el} = 29$: ^1H , D , ^3He , ^4He , ^7Li , ^8Be , ^8B , ^{12}C , ^{13}C , ^{14}N , ^{15}N , ^{16}N , ^{17}N , ^{17}O , ^{18}O , ^{18}F , ^{19}F , ^{20}Ne , ^{21}Ne , ^{22}Ne , ^{23}Na , ^{24}Mg , ^{25}Mg , ^{26}Mg , $^{26}\text{Al}^m$, $^{26}\text{Al}^g$, ^{27}Al , ^{27}Si , and ^{28}Si .

The α -enhanced opacities and equation of state (EOS) are derived for our best estimate of the metal mixture of 47 Tuc, which is described in Sec. 3.1. Details about the preparation of the opacity tables are provided in Bressan et al. (2012). Suffice it to recall that the Rosseland mean opacities come from two sources: from the Opacity Project At Livermore (OPAL, Iglesias & Rogers 1996, and references therein)² team at high temperatures ($4.0 < \log(T/\text{K}) < 8.7$), and from AESOPUS (Marigo & Aringer 2009)³ at low temperatures ($3.2 < \log(T/\text{K}) < 4.1$), with a smooth transition being adopted in the $4.0 < \log(T/\text{K}) < 4.1$ interval. Conductive opacities are provided by Itoh et al. (2008) routines. As for the EOS, we choose the widely used FreeEOS code (version 2.2.1 in the EOS4 configuration)⁴ developed by Alan W. Irwin for its computational efficiency.

It is worth noting here that when we change the heavy element number fractions (N_i/N_Z) to obtain a new metal partition in PARSEC, their fractional abundances by mass (Z_i/Z_{tot}) are normalized in such a way that the global metallicity, Z , is kept constant. Hence, compared to the solar partition at the same total metallicity Z , a model with enhanced α -elements shows a depression of Fe and the related elements, because the total metallicity remains unchanged by construction. The Hertzsprung-Russell diagram (HRD) in the left panel of Fig. 1 shows that, with the same total metallicity Z and helium content Y , the α -enhanced star (orange solid line) is slightly hotter than the solar-scaled one (blue dashed line) both on the main sequence and on the red giant branch because of the net effect of changes to the opacity. Higher temperature leads to a faster evolution, as illustrated in the right panel of Fig. 1. It is also interesting to compare the α -enhanced star to a solar-scaled one with the same $[\text{Fe}/\text{H}]$ (black dotted line in Fig. 1). With the same $[\text{Fe}/\text{H}]$ but higher total metallicity Z , the α -enhanced star is cooler. Indeed, VandenBerg et al. (2012) report that if keeping $[\text{Fe}/\text{H}]$ constant, the giant branch is shifted to a cooler temperature with increased Mg or Si, while O, Ne, S abundances mainly affect the temperatures of main sequence and turn-off phases.

Various initial helium abundance values, for a given metallicity, are allowed in the new version of PARSEC. In the previous versions the initial helium mass fraction of the stars was obtained from the helium-to-metals enrichment law:

$$Y = Y_p + \frac{\Delta Y}{\Delta Z} Z = 0.2485 + 1.78 \times Z \quad (1)$$

where Y_p is the primordial helium abundance (Komatsu et al.

² <http://opalopacity.llnl.gov/>

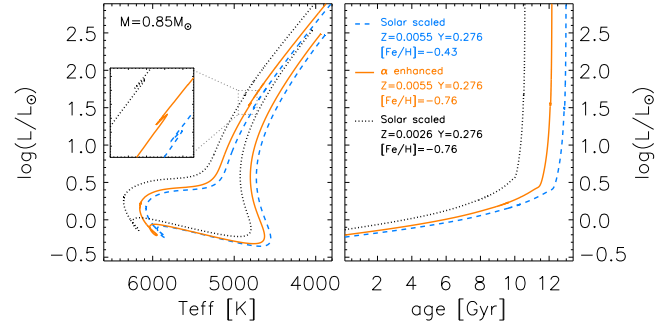
³ <http://stev.oapd.inaf.it/aesopus>

⁴ <http://freeeos.sourceforge.net/>

Table 1. Nuclear reaction rates adopted in this work and the reference from which we take their reaction energy Q .

Reaction	Reference
p(p, β^+ γ) D	Betts, Fortune & Middleton (1975)
p(D, γ) ^3He	Descouvemont et al. (2004)
^3He (^3He , γ) 2p + ^4He	Angulo et al. (1999)
^4He (^3He , γ) ^7Be	Cyburt & Davids (2008)
^7Be (e $^-$, γ) ^7Li	Cyburt et al. (2010)
^7Li (p, γ) ^4He + ^4He	Descouvemont et al. (2004)
^7Be (p, γ) ^8B	Angulo et al. (1999)
^{12}C (p, γ) ^{13}N	Li et al. (2010)
^{13}C (p, γ) ^{14}N	Angulo et al. (1999)
^{14}N (p, γ) ^{15}O	Imbriani et al. (2005)
^{15}N (p, γ) ^4He + ^{12}C	Angulo et al. (1999)
^{15}N (p, γ) ^{16}O	Iliadis et al. (2010)
^{16}O (p, γ) ^{17}F	Iliadis et al. (2008)
^{17}O (p, γ) ^4He + ^{14}N	Iliadis et al. (2010)
^{17}O (p, γ) ^{18}F	Iliadis et al. (2010)
^{18}O (p, γ) ^4He + ^{15}N	Iliadis et al. (2010)
^{18}O (p, γ) ^{19}F	Iliadis et al. (2010)
^{19}F (p, γ) ^4He + ^{16}O	Angulo et al. (1999)
^{19}F (p, γ) ^{20}Ne	Angulo et al. (1999)
^4He (2 ^4He , γ) ^{12}C	Fynbo et al. (2005)
^{12}C (^4He , γ) ^{16}O	Cyburt (2012)
^{14}N (^4He , γ) ^{18}F	Iliadis et al. (2010)
^{15}N (^4He , γ) ^{19}F	Iliadis et al. (2010)
^{16}O (^4He , γ) ^{20}Ne	Constantini & LUNA Collaboration (2010)
^{18}O (^4He , γ) ^{22}Ne	Iliadis et al. (2010)
^{20}Ne (^4He , γ) ^{24}Mg	Iliadis et al. (2010)
^{22}Ne (^4He , γ) ^{26}Mg	Iliadis et al. (2010)
^{24}Mg (^4He , γ) ^{28}Si	Strandberg et al. (2008)
^{13}C (^4He , n) ^{16}O	Heil et al. (2008)
^{17}O (^4He , n) ^{20}Ne	Angulo et al. (1999)
^{18}O (^4He , n) ^{21}Ne	Angulo et al. (1999)
^{21}Ne (^4He , n) ^{24}Mg	Angulo et al. (1999)
^{22}Ne (^4He , n) ^{25}Mg	Iliadis et al. (2010)
^{25}Mg (^4He , n) ^{28}Si	Angulo et al. (1999)
^{20}Ne (p, γ) ^{21}Na	Iliadis et al. (2010)
^{21}Ne (p, γ) ^{22}Na	Iliadis et al. (2010)
^{22}Ne (p, γ) ^{23}Na	Iliadis et al. (2010)
^{23}Na (p, γ) ^4He + ^{20}Ne	Iliadis et al. (2010)
^{23}Na (p, γ) ^{24}Mg	Iliadis et al. (2010)
^{24}Mg (p, γ) ^{25}Al	Iliadis et al. (2010)
^{25}Mg (p, γ) $^{26}\text{Al}^g$	Iliadis et al. (2010)
^{25}Mg (p, γ) $^{26}\text{Al}^m$	Iliadis et al. (2010)
^{26}Mg (p, γ) ^{27}Al	Iliadis et al. (2010)
$^{26}\text{Al}^g$ (p, γ) ^{27}Si	Iliadis et al. (2010)
^{27}Al (p, γ) ^4He + ^{24}Mg	Iliadis et al. (2010)
^{27}Al (p, γ) ^{28}Si	Iliadis et al. (2010)
^{26}Al (p, γ) ^{27}Si	Iliadis et al. (2010)
^{26}Al (n, p) ^{26}Mg	Tuli (2011)
^{12}C (^{12}C , n) ^{23}Mg	Caughlan & Fowler (1988)
^{12}C (^{12}C , p) ^{23}Na	Caughlan & Fowler (1988)
^{12}C (^{12}C , ^4He) ^{20}Ne	Caughlan & Fowler (1988)
^{20}Ne (γ , ^4He) ^{16}O	Constantini & LUNA Collaboration (2010)

2011), and $\Delta Y/\Delta Z$ is the helium-to-metal enrichment ratio. Because of differences in the adopted primordial and solar calibration He and metallicity values by different authors, the above two parameters are slightly different in different stellar evolution codes. The latest YY isochrone (Spada et al. 2013) adopts the relation $Y = 0.25 + 1.48Z$; DSEP (Dotter 2007; Dotter et al. 2007, 2008) uses $Y = 0.245 + 1.54Z$; MIST (Choi et al. 2016)


Figure 1. A comparison between the α -enhanced evolutionary track (orange solid line) and the solar-scaled one with the same metallicity Z (blue dashed line). For comparison, a solar-scaled evolutionary track with the same $[\text{Fe}/\text{H}]$ value (black dotted line) is also displayed. The helium content and the stellar mass of the three stars are the same ($Y=0.276$, $M=0.85 M_{\odot}$). The left panel is HRD with sub-figure zoom-in around the red giant branch bump region. The right panel shows how the luminosity of the star evolve with time.

gives $Y = 0.249 + 1.5Z$, and BaSTI (Pietrinferni et al. 2006) adopts $Y = 0.245 + 1.4Z$. However, observations reveal that the helium content does not always follow a single relation. Differences in helium abundance have been widely confirmed in globular clusters between stellar populations with very similar metallicity. The evidence includes the direct He I measurement on blue horizontal branch star (Villanova, Piotto & Gratton 2009; Mucciarelli et al. 2014; Marino et al. 2014; Gratton et al. 2015, for instance), on giant stars (Dupree, Strader & Smith 2011; Pasquini et al. 2011), and the splitting of sequences in colour-magnitude diagram (CMD) both of globular clusters in Milky Way (e.g. Bedin et al. 2004; Villanova et al. 2007; Piotto et al. 2007; Milone et al. 2008; Di Criscienzo et al. 2010) and in Magellanic Cloud clusters (Milone et al. 2015a, 2016). Bragaglia et al. (2010) found that the brightness of the RGB bump, which should increase with He abundance, is fainter in the first generation than the second generation in 14 globular clusters. Indeed, He variation is considered one of the key parameters (and problems) to understand multiple populations in GCs (see the review by Gratton, Carretta & Bragaglia 2012, and the references therein). In the new version of PARSEC, we allow different helium contents at any given metallicity Z .

3 CALIBRATION WITH 47 TUC

Globular Clusters (GCs) have been traditionally considered as the paradigm of a single stellar population, a coeval and chemically homogeneous population of stars covering a broad range of evolutionary phases, from the low-mass main sequence, to the horizontal branch (HB) and white dwarf sequences. For this reason they were considered the ideal laboratory to observationally study the evolution of low mass stars and to check and calibrate the stellar evolution theory. This picture has been challenged during the last two decades by photometric and spectroscopic evidence of the presence of multiple populations in most, if not all, globular clusters (for instance NGC 6397 (Gratton et al. 2001; Milone et al. 2012), NGC 6752 (Gratton et al. 2001; Milone et al. 2010), NGC 1851 (Carretta et al. 2014), NGC 2808 (D'Antona et al. 2005; Carretta et al. 2006; Piotto et al. 2007; Milone et al. 2015b), NGC

6388 (Carretta et al. 2007), NGC 6139 (Bragaglia et al. 2015), M22 (Marino et al. 2011), etc.). Nevertheless, Globular Clusters remain one of the basic workbenches for the stellar model builders, besides their importance for dynamical studies and, given the discovery of multiple populations, also for the early chemo-dynamical evolution of stellar systems.

47 Tuc, a relatively metal-rich Galactic Globular Cluster, also shows evidence of the presence of at least two different populations: *i)* bimodality in the distribution of CN-weak and CN-strong targets, not only in red giant stars (Briley 1997; Norris & Freeman 1979; Harbeck, Smith & Grebel 2003) but also in MS members (Cannon et al. 1998); *ii)* luminosity dispersion in the sub-giant branch, low-main sequence and HB (Anderson et al. 2009; Di Criscienzo et al. 2010; Nataf et al. 2011; Salaris, Cassisi & Pietrinferni 2016) indicating a dispersion in He abundance; *iii)* anti-correlation of Na-O in RGB and HB stars (Carretta et al. 2009b, 2013; Gratton et al. 2013) and also in MS-TO ones (D’Orazi et al. 2010; Dobrovolskas et al. 2014).

The presence of at least two different populations with different chemical compositions seems irrefutable (even if their origin is still under debate). Particularly convincing is the photometric study by Milone et al. (2012, and references therein), which concludes, in good agreement with other works (Carretta et al. 2009b, 2013), that for each evolutionary phase, from MS to HB, the stellar content of 47 Tuc belongs to two different populations, “first generation” and “second generation” ones (thereafter, FG and SG respectively). The FG population represents $\sim 30\%$ of the stars, and it is more uniformly spatially distributed than the SG population, which is more concentrated in the central regions of the cluster.

Choosing 47 Tuc as a reference to calibrate PARSEC stellar models, requires therefore computation of stellar models with metal mixtures corresponding to the two identified populations. In the next section we describe the sources to derive the two different metal mixtures that will be used for the opacity and EOS tables in the stellar model computations, and in the follow-up isochrone fitting.

3.1 Metal mixtures

Chemical element abundances are given in the literature as the absolute values $A(X)$ ⁵, or as $[X/Fe]$ ⁶, the abundance with respect to the iron content and referred to the same quantity in the Sun. Since the solar metal mixture has changed lately and since there is still a hot debate about the chemical composition of the Sun, it is important to translate all the available data to absolute abundances, taking into account the solar mixture considered in each source. We follow that procedure to derive the metal mixtures for the first and second generation in 47 Tuc.

The separation between the two populations based on photometric colours done by Milone et al. (2012) agree with the separation based on Na-O anti-correlation by Carretta et al. (2009b) and Gratton et al. (2013). We decide hence to use the same criteria to classify the star as FG or SG member.

Concerning He mass fraction Y , the scatter in luminosity seen in some evolutionary phases has been attributed to different amounts of He in the stellar plasma (see references above). The

analyses presented in Milone et al. (2012) suggests that the best fitting of the colour difference between the two populations is obtained with a combination of different C, N and O abundances, plus a small increase of He content in the SG ($\Delta Y=0.015-0.02$). These results agree with those presented in Di Criscienzo et al. (2010, $\Delta Y=0.02-0.03$), and rule out the possibility of explaining the 47 Tuc CMD only with the variation of He abundance.

Table 2 lists the elemental abundances we adopt for the two generations of 47 Tuc together with the corresponding references. The abundances of some elements, like carbon, nitrogen and oxygen, may change during the evolution because of standard (convection) and non-standard (i.e. rotational mixing) transport processes. Therefore, CNO abundances are compiled from available measurements for MS/TO stars, and their sum abundances are nearly the same in both populations. Other elements are not expected to be affected by mixing processes during stellar evolution, so we use the values measured mainly in the red giant phase where hundreds of stars are observed. If available, abundance determinations that take into account NLTE and 3D effects are adopted. There is no clear abundance difference of elements Mg, Al, Si, Ca, and Ti between the two populations of 47 Tuc. Since their abundances show large scatter from different literature sources and are sensitive to the choice of measured lines, we use the mean values of the literature abundances for both FG and SG. The iron abundance $[Fe/H]=-0.76$ dex is adopted from Carretta et al. (2009a) and Gratton et al. (2013) who measure the largest giant sample and HB sample of 47 Tuc respectively with internal fitting errors less than 0.02 dex. The $[Fe/H]$ values derived from giants are much less dependent on the effects of microscopic diffusion than in the case of main sequence stars. We notice that in literature some authors suggest a $[Fe/H]$ dispersion of ~ 0.1 dex for 47 Tuc (Alves-Brito et al. 2005). On the other hand Anderson et al. (2009) conclude that for 47 Tuc a He dispersion of ~ 0.026 has an equal effect on the MS as a $[Fe/H]$ dispersion of ~ 0.1 dex. Since we consider different He contents for the FG and SG stars, we do not apply any further $[Fe/H]$ dispersion. Other elements which are not displayed in table 2 keep the solar abundances ($[X/Fe]=0$). The anti-correlation between the abundances of C and N, as well as O and Na, contributes to the main difference of the metal mixtures between FG and SG. The difference in the final $[\alpha/Fe]$ values between the two generations is due to the difference in O abundance. The resulting metallicities are $Z_{FG} = 0.0056$ for the first generation and $Z_{SG} = 0.0055$ for the second generation, respectively. Following Milone et al. (2012), the assumed He abundances are $Y=0.256$ and $Y=0.276$ for FG and SG, respectively. Table 3 lists the general metal mixture information for the two stellar populations, including Z , Y , $[M/H]$, $[Fe/H]$, and $[\alpha/Fe]$. The referred solar abundance is derived from Caffau et al. (2011), as described in Bressan et al. (2012). We consider eight α elements when calculating the total α enrichment $[\alpha/Fe]$: O, Ne, Mg, Si, S, Ca, Ar, and Ti. Thus for the FG stars of 47 Tuc, $[Z=0.0056, Y=0.256]$, $[\alpha/Fe] = 0.4057$ dex and, for the SG stars, $[Z=0.0055, Y=0.276]$, $[\alpha/Fe] = 0.2277$ dex. These two values, approximately ~ 0.4 and 0.2 respectively, are the typical $[\alpha/Fe]$ values observed in α -enriched stars. Finally we note that we will adopt the metal partitions of these two α -enriched generations to calculate stellar evolutionary tracks and isochrones also for other metallicities.

3.2 Isochrones fitting and Luminosity function

With the detailed metal mixture and helium abundance of 47 Tuc, we calculate new sets of evolutionary tracks and isochrones, and transform them into the observational color-magnitude diagram

⁵ $A(X) = \log(N_X/N_H) + 12$, with N_X is the abundance in number for the element X.

⁶ $[X/Fe]=\log(N_X/N_{Fe}) - \log(N_X/N_{Fe})_\odot$

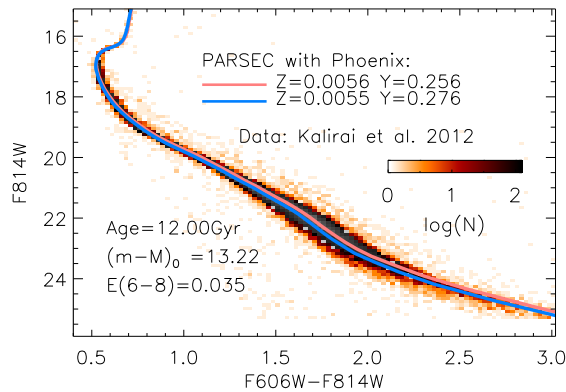
Table 2. Chemical element abundances of 47 Tuc two stellar populations (FG and SG). The abundances are written in the format of [X/Fe], their corresponding references are also listed.

	FG	SG	reference	note
[C/Fe]	0.12	-0.09	Cannon et al. (1998); Milone et al. (2012)	MS
[N/Fe]	0.32	1.17	Cannon et al. (1998); Milone et al. (2012)	MS
[O/Fe]	0.42	0.17	Dobrovolskas et al. (2014)	TO, NLTE+3D
[Ne/Fe]	0.40	0.40	—	estimated
[Na/Fe]	-0.12	0.10	Dobrovolskas et al. (2014)	TO, NLTE+3D
[Mg/Fe]	0.32	0.32	Carretta et al. (2009b, 2013); Gratton et al. (2013); Cordero et al. (2014); Thygesen et al. (2014)	mean value of RGB/HB
[Al/Fe]	0.20	0.20	Cordero et al. (2014); Thygesen et al. (2014)	mean value of RGB
[Si/Fe]	0.27	0.27	Gratton et al. (2013); Thygesen et al. (2014); Carretta et al. (2009b); Cordero et al. (2014)	mean value of RGB/HB
[S/Fe]	0.40	0.40	—	estimated
[Ca/Fe]	0.27	0.27	Carretta et al. (2009b); Gratton et al. (2013); Cordero et al. (2014); Thygesen et al. (2014)	mean value of RGB/HB
[Ti/Fe]	0.20	0.20	Cordero et al. (2014); Thygesen et al. (2014)	mean value of RGB/HB

Table 3. General metal mixture of 47 Tuc two stellar populations (FG and SG).

	FG	SG
Z	0.0056	0.0055
Y	0.256	0.276
[M/H]	-0.43	-0.41
[Fe/H]	-0.76	-0.76
[α /Fe] [†]	0.41	0.23

[†] Labeled as [α /Fe] \sim 0.4 and 0.2. Difference in the [α /Fe] values is due to O abundance differences.


Figure 2. Isochrone fitting with Hess diagram of 47 Tuc data for the low main sequence (Kalirai et al. 2012). The bin size of Hess diagram is 0.025 mag in color and 0.1 mag in F814W magnitude. The fitting parameters (age, η , $(m-M)_0$, and $E(6-8)$) are listed in the legend.

(CMD) in order to fit the data. This fitting procedure, based on our adopted model prescriptions (e.g. mixing length, atmospheric boundary condition, bolometric corrections), aims to calibrate other parameters (e.g. extra mixing) in the model as described below.

3.2.1 Low main sequence to turn-off

Kalirai et al. (2012) provides deep images of 47 Tuc taken with the Advanced Camera for Surveys (ACS) on *Hubble Space Telescope* (HST). The corresponding colour-magnitude diagrams cover the whole main sequence of this cluster, till the faintest stars. Fig. 2 shows our isochrone fitting of their photometric data, i.e. in the

F606W and F814W bands. In order to display the relative density of stars on CMD the data are plotted with the Hess diagram (bin-size 0.025 mag in color and 0.1 mag in I magnitude). By assuming a standard extinction law (Cardelli, Clayton & Mathis 1989) we derive, from the isochrone fitting, an age of 12.00 Gyr, a distance modulus $(m-M)_0$ of 13.22 ($(m-M)_{F606W} \sim 13.32$), and a reddening of $E(F606W-F814W)=0.035$ (hereafter named $E(6-8)$). The fitting is performed not only to the main sequence but also to the giant branch and HB phase as we will show later in Sec. 3.2.3 and Sec. 3.2.4. The values of age, $(m-M)_0$, and $E(6-8)$ are adjusted with visual inspection with the priority of improving the turn-off and HB fittings.

The distance modulus of 47 Tuc has been determined by many other authors, however with different results. For instance, using HST proper motion Watkins et al. (2015) derive a distance of 4.15 kpc ($(m-M)_0 \sim 13.09$) which is lower than the values in the Harris catalog (4.5 kpc ($(m-M)_0 \sim 13.27$) and $(m-M)_V=13.37$, Harris 1996, 2010 edition); the eclipsing binary distance measurement ($(m-M)_V=13.35$, Thompson et al. 2010); the result based on the white dwarf cooling sequence ($(m-M)_0 \sim 13.32$, Hansen et al. 2013); and that derived from isochrone fitting to BVI photometry ($(m-M)_V=13.375$, Bergbusch & Stetson 2009). Our best fit distance lies in between them, and agrees with other recent distance modulus determinations (e.g. Brogaard et al. 2017, $(m-M)_0=13.21 \pm 0.06$ based on the eclipsing binary). *Gaia* will release the parallaxes and proper motions including stars in 47 Tuc in its DR2 in early 2018, and will help to solve the distance problem. However, we will show in the following section that our best estimate result offers a very good global fitting, from the very low main sequence till the red giant and horizontal branches.

3.2.2 RGB bump and envelope overshooting calibration

Some GC features in CMD are very sensitive to stellar model parameters which are, otherwise, hardly constrained from observations directly. This is the case of the efficiency of mixing below the convective envelope (envelope overshooting), that is known to affect the luminosity of the red giant branch bump (RGBB). In this section we will use the 47 Tuc data to calibrate the envelope overshooting to be used in low mass stars by PARSEC.

The RGB bump is one of the most intriguing features in the CMD. When a star evolves to the “first dredge-up” in the red giant phase, its surface convective zone deepens while the burning hydrogen shell moves outwards. When the hydrogen burning shell encounters the chemical composition discontinuity left by the pre-

vious penetration of the convective zone, the sudden increase of H affects the efficiency of the burning shell and the star becomes temporarily fainter. Soon after a new equilibrium is reached, the luminosity of the star raises again. Since the evolutionary track crosses the same luminosity three times in a short time, there is an excess of star counts in a small range of magnitudes, making a “bump” in the star number distribution (Luminosity Function) along the red giant branch. This is because the number of stars in the post main sequence phases is proportional to the evolutionary time of the stars in these phases. The longer the crossing time of the chemical composition discontinuity by the burning shell, the more the stars accumulate in that region of the RGB.

The properties of RGBB, including the brightness and the extent, are important to study the stellar structure and to investigate the nature of GCs. 47 Tuc was the first GC where the existence of the RGBB was confirmed (King, Da Costa & Demarque 1985). Since then, many works, both theoretical and observational (for instance, Alongi et al. 1991; Cassisi & Salaris 1997; Zoccali et al. 1999; Bono et al. 2001; Cassisi, Salaris & Bono 2002; Bjork & Chaboyer 2006; Salaris et al. 2006; Cecco et al. 2010; Bragaglia et al. 2010; Cassisi et al. 2011; Nataf et al. 2013), have studied the features of RGBB.

The intrinsic brightness and extent of the RGBB are sensitive to:

Total metallicity and metal partition: Nataf et al. (2013) propose an empirical function of RGBB extent to metallicity: the more metal-poor the globular cluster is, the smaller is the extent of the RGBB. From the theoretical point of view, stars with lower total metallicity are brighter compared to the higher metallicity stars, causing their hydrogen burning shell to move outwards faster. Since they are also hotter, the surface convective envelope is thinner and the chemical composition discontinuity is smaller and less deep. As a consequence, their RGBB is very brief and covers a small range of magnitudes at higher luminosity. This is why RGBB in metal-poor globular clusters is very difficult to be well sampled. The metal partition also affects the features of RGBB, even with the total metallicity remains the same. As already shown in Fig. 1 and in Sec. 2, a stellar track with α -enhancement is hotter than the solar-scaled one with the same total metallicity Z because of different opacity, leading to a brighter RGBB. Since CNO are the most affected elements in the giant branch and they are important contributors to the opacities, their varying abundances have an important impact on the location of RGBB. e.g. Rood & Crocker (1985) shows that enhancing CNO by a factor of ten has larger effect on the RGBB luminosity than enhancing Fe by a factor of ten over the same metallicity Z . More recently, VandenBerg (2013) show that higher oxygen abundance leads to a fainter RGBB if the [Fe/H] is fixed.

Helium content: A larger helium content renders the star hotter and brighter (Fagotto et al. 1994). Bragaglia et al. (2010) studied the RGBB of 14 globular clusters and found that the more He-rich second generation shows brighter RGBB than the first generation. Similar to the mechanism in metal-poor stars, hot He-rich stars have less deep convective envelopes and their high luminosity makes the hydrogen burning shells to move faster across the discontinuity. Hence with the same total metallicity Z and stellar mass the RGBB of the He-rich star is brighter, less extended, and more brief. In table 4 we take a $M=0.85 M_{\odot}$ star as an example to show how the RGBB luminosity and evolution time vary with different helium contents.

Age: Stars with younger age are hotter, with their thinner convective

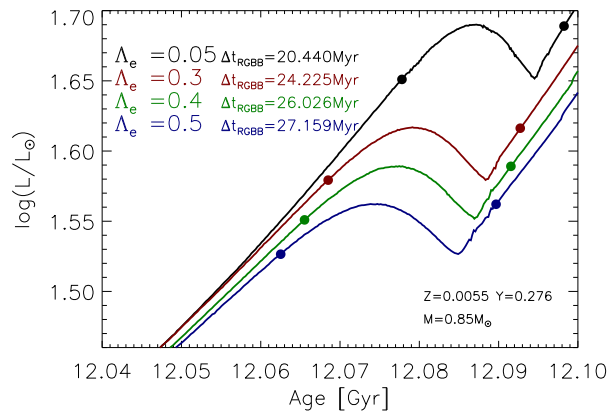


Figure 3. The RGBB luminosity as a function of stellar age for a $0.85 M_{\odot}$ star but with different EOV. The black, red, green, and blue line from top to bottom represent tracks with $\Lambda_e = 0.05, 0.3, 0.4,$ and 0.5 . The filled dots mark the minimum and maximum luminosity of RGBB for each track, and Δt_{RGBB} is the evolution time from the minimum luminosity to the maximum one.

envelope their RGBB are brighter. In principle multiple populations born in different ages spread the GC RGBB luminosity. However, considering that the age variation of the multiple populations is usually small (\sim a few Myr), it contributes little to the GC RGBB luminosity spread compared to the He variation (see, e.g. Nataf et al. 2011).

Mixing efficiency: The mixing efficiency of the star, both mixing length and envelope overshooting (EOV), determines the maximum depth of the convective envelope and affects the brightness and evolutionary time of RGBB. The more efficient the mixing is, the deeper the convective envelope is, the earlier the hydrogen-burning shell meets the discontinuity left by the penetration of the surface convective zone and the fainter the RGBB is. For the mixing length, we adopt the solar-calibrated value $\alpha_{MLT}^{\odot}=1.74$ in PARSEC as described in (Bressan et al. 2012). The EOV is calibrated with the new stellar tracks against the observations of the RGBB of 47 Tuc.

Overshooting is the non-local mixing that may occur at the borders of any convectively unstable region (i.e., Bressan et al. 2015, and references therein). The extent of the overshooting at the base of the convective envelope is called envelope overshooting, and the one above the stellar convective core is called core overshooting. There are observations that can be better explained with envelope overshooting, for instance, the blue loops of intermediate and massive stars (Alongi et al. 1991; Tang et al. 2014), and the carbon stars luminosity functions in the Magellanic Clouds, that require a more efficient third dredge-up in AGB stars (Herwig 2000; Marigo & Girardi 2007). At the base of the convective envelope of the Sun, models with an envelope overshooting of $\Lambda_e \approx 0.3 \sim 0.5 H_p$ (where H_p is the pressure scale height) provide a better agreement with the helioseismology data (Christensen-Dalsgaard et al. 2011). The envelope overshooting also affects the surface abundance of light elements (Fu et al. 2015), and asteroseismic signatures in stars (Lebreton & Goupil 2012).

In Fig. 3 we compare the RGBB evolution of models computed with different EOV values, Λ_e , at the same stellar mass and composition. Every pair of filled dots marks the brightness extent of the RGBB. The figure shows that a larger envelope overshoot-

Table 4. RGBB parameters of stars with a constant mass ($M=0.85 M_{\odot}$) and metallicity ($Z=0.0055$) but different helium contents. Mean luminosity $\log(\bar{L}/L_{\odot})_{\text{RGBB}}$, luminosity extent $\Delta \log(L)_{\text{RGBB}}$, RGBB beginning time $t_{0,\text{RGBB}}$, and RGBB lifetime Δt_{RGBB} are listed.

Z	Y	$\log(\bar{L}/L_{\odot})_{\text{RGBB}}$	$\Delta \log(L)_{\text{RGBB}}$	$t_{0,\text{RGBB}}$ (Gyr)	Δt_{RGBB} (Myr)
0.0055	0.276	1.5443	0.03557	12.062	27.159
0.0055	0.296	1.5887	0.03177	10.584	22.637

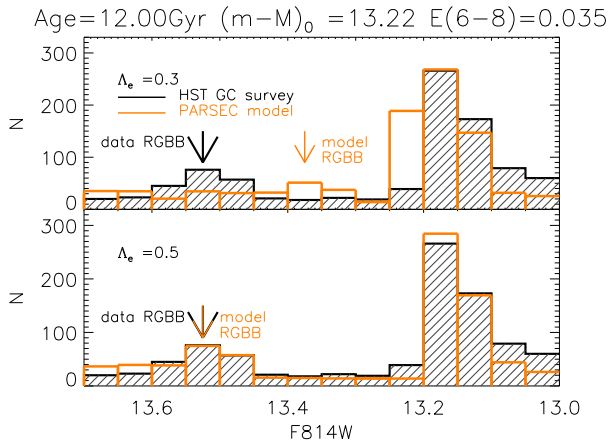


Figure 4. Comparison between LF of 47 Tuc data (Sarajedini et al. 2007) and the new PARSEC isochrone with different EOJ. The fitting parameters (age, $(m-M)_0$, and $E(6-8)$) the same as in Fig. 2. The black histogram filled with oblique lines is the data LF, whilst orange histogram is LF derived from new PARSEC isochrones with 30% contribution from the FG of 47 Tuc and 70% from the SG. The upper panel isochrones of each sub-figure are calculated with EOJ value $\Lambda_e=0.3$, and the lower panel are the ones with $\Lambda_e=0.5$. Orange arrow and black arrow mark the location of RGBB in model and in data, respectively. The bin size of the LF is 0.05 mag.

ing not only makes the RGBB fainter, but also of longer duration, leading to a more populated RGBB. A larger EOJ value leads to a deeper surface convective zone, and the hydrogen burning shell encounters the chemical discontinuity earlier.

The Luminosity Function (LF) is a useful tool to compare the observed morphology of RGBB with that predicted by the theory. Taking into account that the 47 Tuc population contribution is 30% from the FG and 70% from the SG as suggested by Milone et al. (2012) and Carretta et al. (2009b), we simulated the LF of 47 Tuc with our isochrones with different EOJ values. The comparison between the observed and predicted LFs is shown in Fig. 4. For the observed LF we have used data from the HST/ACS survey of globular clusters (Sarajedini et al. 2007). Both observations and models are sampled in bins of 0.05 magnitudes. The fitting parameters are the same as those we used in Fig. 2. The model LF (orange histogram) are calculated with envelope overshooting $\Lambda_e=0.3$ in the upper panel and with $\Lambda_e=0.5$ in the lower panel. It is evident that the LF computed with the small envelope overshooting value $\Lambda_e=0.3$ has RGBB too bright compared to data (black histogram filled with oblique lines). We find that the agreement between observations and models is reached when one adopts a value of $\Lambda_e = 0.5H_p$ below the convective border, with our adopted metal mixtures and best fit isochrone. This provides a robust calibration of the envelope overshooting parameter. This envelope overshooting calibration will be applied to all other stellar evolution calculations of low mass stars.

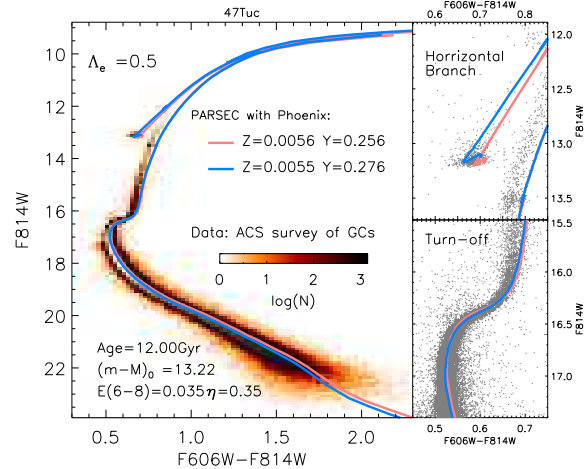


Figure 5. Isochrone fitting with Hess diagram (the left panel) of 47 Tuc data (Sarajedini et al. 2007) for all the evolutionary phases, and with scatter plots highlighting the horizontal branch region (the upper right panel) and the turn-off region (the lower right panel). The red line and blue line represent isochrones of the first and second generation, respectively, as the legend shows. The fitting parameters are: age=12.00 Gyr, $(m-M)_0=13.22$, $E(6-8)=0.035$.

3.2.3 Red Giant Branch

While Kalirai et al. (2012) focus on the faint part of the main sequence as shown in Fig. 2, another dataset of 47 Tuc, the HST/ACS survey of globular clusters (Sarajedini et al. 2007), is devoted to the Horizontal Branch (Anderson et al. 2008) with the same instrument. In Fig. 5 we show the global fitting of ACS data of 47 Tuc, from main sequence up to the red giant branch and HB. The best fitting parameters we derived are the same as those we used to fit the lower main sequence data in Fig. 2. The Hess diagram is used for the global fitting (the left panel) with bin size 0.025 mag in color and 0.1 mag in F814W magnitude. The HB region and the turn-off region are zoomed in with scatter plots in the two right panels. Thanks to the detailed composition derived from the already quoted observations for the two main populations of 47 Tuc and the new computed models, by assuming a standard extinction law (Cardelli, Clayton & Mathis 1989) and using the adopted EOJ and mixing length parameters, we are able to perform a global fit to the CMD of 47 Tuc covering almost every evolutionary phase over a range of about 13 Magnitudes. This must be compared with other fittings that can be found in literature and that usually are restricted to only selected evolutionary phases (Kim et al. 2002; Salaris et al. 2007; VandenBerg et al. 2013, 2014; Chen et al. 2014; McDonald & Zijlstra 2015, etc.). However, it is worth noting that the distance of this cluster, as already discussed in Sec. 3.2.1, together with the cluster age, have varied over the years in many careful studies. We look forward to *Gaia* DR2 to put more constraints to this problem.

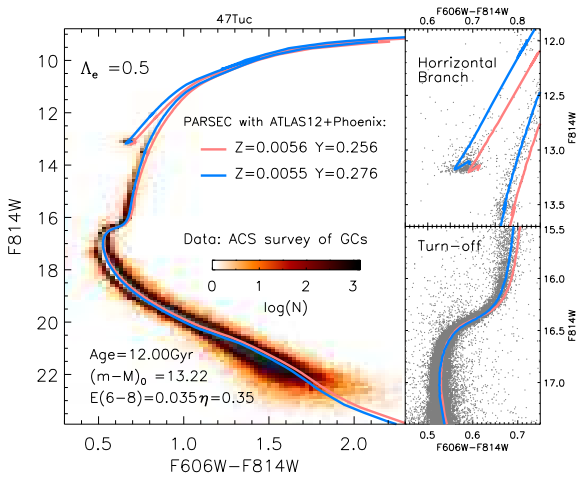


Figure 6. The same isochrone fitting with Hess diagram and scatter plots of 47 Tuc data (Sarajedini et al. 2007) as in Fig. 5, but with atmosphere models from ATLAS12 for Teff hotter than 4000 K.

As the upper right panel of Fig. 5 show, the isochrones corresponding to both of the two stellar generations run on the red side of the data in the RGB phase. Part of the discrepancy could be explained by the bolometric correction used. Here we are using bolometric correction from PHOENIX atmosphere models as described in Chen et al. (2015) for PARSEC v1.2S, where only the total metallicity is considered in the transformation of $\log(L)$ vs. $\log(\text{Teff})$ into F814W vs. (F606W-F814W). As the metallicities of the two 47 Tuc populations ($Z=0.0056$ and $Z=0.0055$) show only a marginal difference, we adopt for the two populations the same bolometric corrections. Thus Fig. 5 reflects basically the difference of the two populations in the theoretical $\log(L)$ vs. $\log(T_{\text{eff}})$ HR diagram. This “RGB-too-red” problem also exists in Dotter et al. (2007), when they fit the same set of data using DSEP models (see their Figure 12), as they apply bolometric correction from PHOENIX as well.

To minimize this discrepancy, we use the ATLAS12 code (Kurucz 2005), which considers not only the total metallicity Z but also $\log(g)$ and detailed chemical compositions for the color transformation, to compute new atmosphere models with our best estimate chemical compositions of the two 47 Tuc populations. We adopt these ATLAS12 models for the new fits to 47 Tuc, but only for models with Teff hotter than 4000 K ((F606W-F814W) ~ 1.3). For lower Teff we still use PHOENIX because ATLAS12 models may be not reliable at cooler temperatures (Chen et al. 2014). Here we show the fit obtained with ATLAS12+PHOENIX bolometric correction in Fig. 6. We see that with the same fitting parameters as in Fig. 5, the prediction of the RGB colors is improved by applying new ATLAS12 bolometric correction. The two stellar generation are split on RGB phase in Fig. 6. We see that the SG ($Z=0.0055$), which is the main contributor as suggested by Milone et al. (2012) and Carretta et al. (2009b), is consistent with the denser region of the RGB data. In other evolutionary phases the new ATLAS12 bolometric corrections do not bring noticeable changes.

Since ATLAS12 only slightly affects the color of the RGB base, and the remainder of this paper deals with the LF of the bump and of the HB, in the following discussion, we will continue to use the standard atmosphere models of PARSEC v1.2S. PARSEC isochrones with ATLAS12 atmosphere models will be discussed in detail in another following work (Chen et al. in prep.)

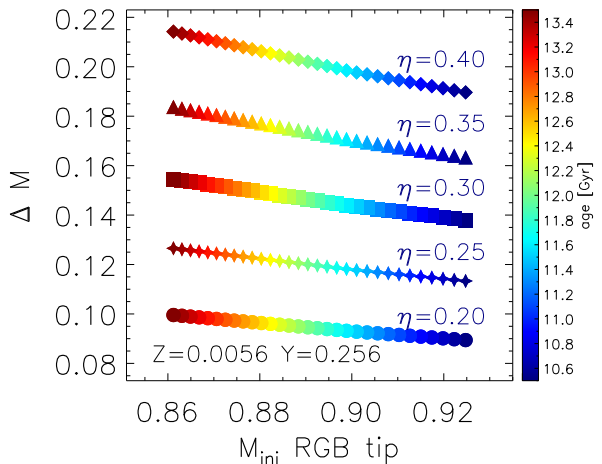


Figure 7. RGB mass lost in unit of M_{\odot} for FG of 47 Tuc ($Z=0.0056$, $Y=0.256$). The X axis is the initial mass of the tip RGB star, and the Y axis shows the mass lost in this star during RGB phase. Five different efficiency factors η are illustrated, from top to bottom $\eta=0.40$ (filled diamond), $\eta=0.35$ (filled triangle), $\eta=0.30$ (filled square), $\eta=0.25$ (filled star), and $\eta=0.20$ (filled dots). The color code displays the age, as shown in the color bar.

Mass loss by stellar winds during the RGB phase has been considered for low mass stars, using the empirical formula by Reimers (1975) multiplied by an efficiency factor η . In Fig. 7 we show the mass lost by RGB stars in unit of M_{\odot} for the FG of 47 Tuc (the plot for SG is very similar). Different efficiency factors (η) and ages are applied. ΔM in the figure is the difference between the initial mass and current mass of the tip RGB star: $\Delta M = M_{\text{initial}} - M_{\text{current}}$. The lost mass, which is greater with larger η , is an increasing function of the cluster age. It is very difficult to derive observationally the mass lost in RGB stars directly since an accurate mass is not easy to derive and the RGB tip is hard to identify. However, the RGB mass loss characterises the HB morphology, and this will be discussed in next section.

3.2.4 Horizontal Branch morphology

The morphology of the Horizontal Branch in globular clusters is widely studied since the “second parameter problem” (that is, the colour of the HB is determined not only by metallicity, van den Bergh 1967; Sandage & Wildey 1967) was introduced. Aside from metallicity as the “first parameter”, age, He content, mass-loss, and cluster central density have been suggested as candidates to be the second, or even third, parameter affecting the morphology of the HB (Fusi Pecci & Bellazzini 1997; Catelan 2008; Dotter et al. 2010; Gratton et al. 2010; McDonald & Zijlstra 2015; D’Antona et al. 2002; Caloi & D’Antona 2005, .etc.). Most of these parameters involve an effect on the mass of the stars which populate the cluster HB. Stars with smaller stellar mass are hotter in temperature and bluer in color. The HB stellar mass decreases as the cluster ages. At a given age, He-rich star evolves faster and reach the Zero-Age Horizontal Branch (ZAHB) with lower mass. If the age and He content are the same, the mass of HB stars is fixed by the mass loss along the RGB (here the mass loss driven by the helium flash is not considered). Although the RGB mass loss does not significantly affect the RGB evolutionary tracks, it determines

the location of the stars on the HB, by tuning the stellar mass. Here we illustrate how helium content and the RGB mass loss affect the HB morphology in the case of 47 Tuc.

The HB morphology with five different values of η is displayed in Fig. 8 for our best fitting parameters derived in Sec. 3.2.3. Different metal/helium abundances ($[Z=0.0056, Y=0.256]$, $[Z=0.0055, Y=0.276]$, $[Z=0.0056, Y=0.276]$, and $[Z=0.0055, Y=0.296]$) are displayed. The isochrones with $Z=0.0056$ are calculated with $[\alpha/Fe] \sim 0.4$ and those with $Z=0.0055$ are calculated with $[\alpha/Fe] \sim 0.2$. The 47 Tuc data (Sarajedini et al. 2007) are also plotted for comparison. The differences between the isochrone with $[Z=0.0055, Y=0.276]$ (blue solid line) and the one with $[Z=0.0056, Y=0.276]$ (orange dashed line) are negligible on the HB, even though they refer to a different α -enhanced mixture. With the same RGB mass loss factor η , He-rich stars have their HB more extended (because of smaller stellar mass), bluer (due to both the smaller stellar mass and the He-rich effect on radiative opacity), and more luminous (because of larger He content in the envelope). For stars with larger mass loss efficiency η during their RGB phase, their HB is bluer, fainter, and more extended, because of smaller stellar mass (hence smaller envelope mass, since the core mass does not vary significantly with the mass loss rate). Indeed, the effects of a higher He content and of a lower mass (no matter if it is the result of an older age or a larger RGB mass loss) on HB stars are difficult to distinguished by means of the color, but can be disentangled because the larger helium content makes the He-rich star slightly more luminous.

Table 5 lists the current mass, M_{ZAHB} , of the first HB star and the corresponding mass that has been lost ΔM_{RGB} , in unit of M_{\odot} . In the table we also show the HB mass range δM_{HB} that produces the corresponding color extent of HB. All cases displayed in Fig. 8 are itemized.

If one considers a uniform mass loss parameter η for the two populations of 47 Tuc ($[Z=0.0056, Y=0.256]$, and $[Z=0.0055, Y=0.276]$), $\eta = 0.35$ is the value that fits better the HB morphology in our best fitting case, as Fig. 8 illustrates. As shown in Table 5, a RGB mass loss parameter of $\eta = 0.35$ leads to a value of the mass lost during RGB between $0.1737 M_{\odot}$ – $0.1755 M_{\odot}$. In the literature there is a discrepancy among the results on RGB mass loss derived with different approaches, namely: cluster dynamics, infrared excess due to dust, and HB modelling for this cluster. Heyl et al. (2015) study the dynamics of white dwarf in 47 Tuc, and concluded that the mass lost by stars at the end of the RGB phase should be less than about $0.2 M_{\odot}$. Origlia et al. (2007) observe the circumstellar envelopes around RGB stars in this cluster from mid-IR photometry and find the total mass lost on the RGB is $\approx 0.23 \pm 0.07 M_{\odot}$. McDonald & Zijlstra (2015) use HB star mass from literature to study the RGB mass loss and derive a Reimers factor $\eta = 0.452$ (corresponding to a RGB mass loss greater than $\sim 0.20 M_{\odot}$). Most recently, Salaris, Cassisi & Pietrinferni (2016) assume a distribution of the initial He abundance to simulate the observed HB of 47 Tuc. They derive a lower limit to the RGB mass loss of about $0.17 M_{\odot}$, but larger values are also possible, up to $0.30 M_{\odot}$, with younger age, higher metallicity and reddening. Our RGB mass loss results, based on a uniform mass loss parameter and our best fitting case of the two populations of this cluster, is consistent with the lower and upper limit values from the literature. However, the real situations of the RGB mass loss in GCs, as discussed in the references above, could be much more complicated. In our final database of the new PARSEC isochrones we will provide different choices of He contents and mass loss parameters for the users' science purpose.

Table 5. The mass lost during the RGB in unit of M_{\odot} for different η and metal/helium abundance. The current mass of the first HB star is M_{ZAHB} , and ΔM_{RGB} represents its RGB mass loss in unit of M_{\odot} . The HB mass range is itemized in the last column δM_{HB} . All values listed here are derived from isochrones with age=12.0 Gyr, $(m-M)_0=13.22$, and $E(V-I)=0.035$, as shown on Fig. 8.

Z	Y	η	$M_{ZAHB} (M_{\odot})$	$\Delta M_{RGB} (M_{\odot})$	$\delta M_{HB} (M_{\odot})$
0.0056	0.256	0.20	0.795832	0.0946	0.0023
		0.25	0.770375	0.1201	0.0033
		0.30	0.744052	0.1464	0.0044
		0.35	0.716765	0.1737	0.0053
		0.40	0.688402	0.2020	0.0059
0.0055	0.276	0.20	0.758027	0.0953	0.0029
		0.25	0.732270	0.1211	0.0039
		0.30	0.705582	0.1478	0.0051
		0.35	0.677852	0.1755	0.0061
		0.40	0.648949	0.2044	0.0067
0.0056	0.276	0.20	0.763649	0.0948	0.0028
		0.25	0.738049	0.1204	0.0039
		0.30	0.711533	0.1470	0.0050
		0.35	0.683996	0.1745	0.0059
		0.40	0.655309	0.2032	0.0066
0.0055	0.296	0.20	0.726732	0.0954	0.0035
		0.25	0.700873	0.1213	0.0047
		0.30	0.674033	0.1481	0.0058
		0.35	0.646090	0.1760	0.0066
		0.40	0.616896	0.2052	0.0067

The LFs from the turn-off to the HB with a RGB mass loss parameter $\eta = 0.35$ are displayed in Fig. 9 for our best fitting parameters. For comparison, the LF of HST GC survey data (Sarajedini et al. 2007) is also plotted (black histogram filled with oblique lines) with the same binsize 0.05 mag. We adopt the Salpeter IMF (Salpeter 1955) to generate LFs though, as discussed in Sec. 3.2.2, LFs in this phase are not sensitive to IMF because the stellar mass varies very little. LFs are instead sensitive to the evolution time along the phase. All model LFs are normalized to the total number of observed RGB stars within a range of F814W magnitude between 14 mag - 16 mag. The left panels of Fig. 9 show the LFs from the turn-off to the HB, for a 100% FG (red histogram), a 100% SG (blue histogram), and the percentage adopted in Sec. 3.2.2, 30% from FG and 70% from SG (orange histogram), respectively. With our best isochrone fitting parameters, age=12.00 Gyr, $(m-M)_0=13.22$, $E(6-8)=0.035$, $\eta=0.35$, and the population percentage obtained from literature (Carretta et al. 2009b; Milone et al. 2012), the model LF (orange histogram in each figure) show a very good agreement with the observed LF. The three right panels in Fig. 9 are zoomed in on the HB and RGBB regions. The total number of HB stars within 12.9 - 13.3 mag in the observations and in the models are listed in the figure. Since the LF is directly proportional to the evolution time, the good agreement of LF between model and observation in Fig. 9 indicates that the hydrogen shell burning lifetime is correctly predicted in PARSEC.

4 COMPARISON WITH OTHER MODELS AND GC DATA

The new PARSEC α enhanced isochrones provide a very good fit of the color magnitude diagram of 47 Tuc in all evolutionary stages from the lower main sequence to the HB. The location of the RGB

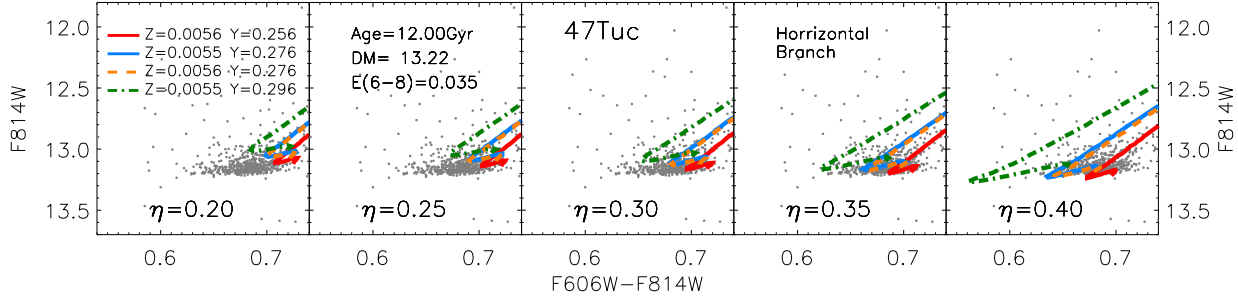


Figure 8. Horizontal branch morphology for different RGB mass loss parameters (η) and metal/helium abundances, with the same isochrone fitting parameters (age, $(m-M)_0$, and $E(6-8)$) as in Fig. 5. The red solid line, blue solid line, orange dashed line, and green dash-dot line represent isochrones of $[Z=0.0056, Y=0.256]$, $[Z=0.0055, Y=0.276]$, $[Z=0.0056, Y=0.276]$, and $[Z=0.0055, Y=0.296]$, respectively. The mass lost during the RGB in unit of M_\odot for each η and metal/helium abundance is listed in Table 5.

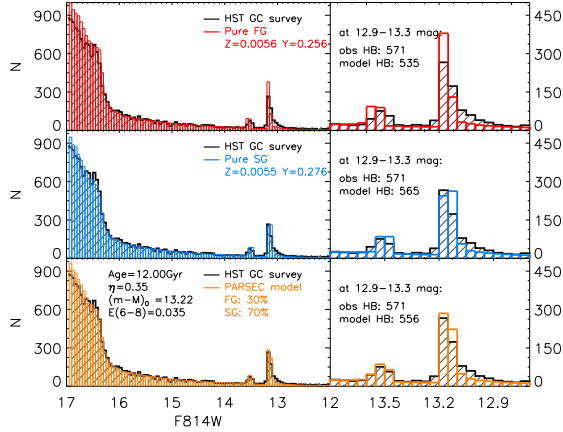


Figure 9. Comparison between the luminosity function of 47 Tuc data (Sarajedini et al. 2007) and that derived from the new PARSEC models, from the turn-off to the HB. The Y axis represent the star counts in magnitude F814W. The black histogram filled with oblique lines is the data LF, whilst the red histogram in the upper panel, blue histogram in the middle panel, and orange histogram in the lower panel, represent 100% FG of 47 Tuc $[Z=0.0056, Y=0.256]$, 100% SG $[Z=0.0055, Y=0.276]$, and their mix with 30% from the FG and 70% from the SG, respectively. The three panels on the right side show the LF of the RGBB and the HB region, for each population mixture. The fitting parameters are: $\eta=0.35$, age=12 Gyr, $(m-M)_0=13.22$, and $E(6-8)=0.035$.

bump shows that the efficiency of the envelope overshoot is quite significant, requiring EOV of $\Lambda_e = 0.5H_p$. This can be considered a calibration of this phenomenon. We now use the calibrated EOV value to obtain α -enhanced isochrones of different metallicities. For this purpose we adopt the partition of heavy elements of the two stellar generations of 47 Tuc ($[\alpha/Fe] \sim 0.4$ and 0.2). In this section we compare our new α -enhanced models with isochrones from other stellar evolution groups and GC data of different metallicities.

4.1 Comparison with other models

The RGBB of globular clusters, as already said in section 3.2.2, has been studied over 30 years since the 47 Tuc RGBB was observed in

1985 (King, Da Costa & Demarque 1985). However, there is a discrepancy between the observed brightness of RGBB and the model predictions: the model RGBB magnitude is about 0.2–0.4 mag brighter than the observed one (Fusi Pecci et al. 1990; Cecco et al. 2010; Troisi et al. 2011). This discrepancy becomes more pronounced in metal-poor GCs (Cassisi et al. 2011).

Here we compare the RGBB magnitude of our newly calibrated PARSEC models with other α -enhanced stellar tracks. Since the BaSTI (Pietrinferni et al. 2006, 2013) and DSEP (Dotter 2007; Dotter et al. 2008) isochrones are publicly available online, we download the $[\alpha/Fe] = 0.4$ isochrones at 13 Gyr from BaSTI Canonical Models database and DSEP web tool 2012 version. We then compare the mean values of their absolute RGBB magnitude in the F606W (HST ACS/WFC) band, with our models. Fig. 10 shows this comparison as a function of total metallicity $[M/H]$ and iron abundance $[Fe/H]$. The model $[M/H]$ is approximated by:

$$[M/H] \approx \log \frac{Z/X}{Z_\odot/X_\odot} \quad (2)$$

And for both of the two new PARSEC models with α enhancement, $[Fe/H] \approx [M/H] - 0.33$. The solar metallicity in PARSEC is $Z_\odot = 0.01524$ and $Z_\odot/X_\odot = 0.0207$. Since DSEP models do not provide $[M/H]$ directly but only $[Fe/H]$ in their isochrones, we calculate $[M/H]$ following Eq. 2 with total metallicity Z , He content Y , and solar Z_\odot/X_\odot taken from their models. Additionally, two PARSEC models with solar-scaled metal mixture ($[\alpha/Fe] = 0$), PARSEC v1.2S and PARSEC with EOV calibration from this work $\Lambda_e = 0.5H_p$, are also plotted. Compared with the new set of solar-scaled PARSEC model with $\Lambda_e = 0.5H_p$ (dark blue line with diamond), the α -enhanced one (red line with triangle) at the same $[M/H]$ (thus same Z and Y) is slightly brighter as we have already discussed in Sec. 2. We notice that the RGBB behavior of PARSEC v1.2S in this figure is different from Figure 3 of Joyce & Chaboyer (2015), which compares PARSEC v1.2S with other models. The reason for this disagreement is unclear to us.

Among the factors that may affect the brightness of the RGBB, as summarized in Sec. 3.2.2, we list the mixing efficiency and He contents. The helium-to-metal enrichment law of the different models are different, as discussed in Sec. 2. PARSEC ($Y = 0.2485 + 1.78Z$) uses a slightly higher He abundance (~ 0.002) than the other two models (BaSTI: $Y = 0.245 + 1.4Z$, DSEP: $Y = 0.245 + 1.54Z$). Different model also adopts different mixing length parameters. The PARSEC mixing length parameter is $\alpha_{MLT} = 1.74$, BaSTI uses $\alpha_{MLT} = 1.913$, and DSEP adopts $\alpha_{MLT} = 1.938$. If all other parameters are the same, a higher He content and a smaller mixing length

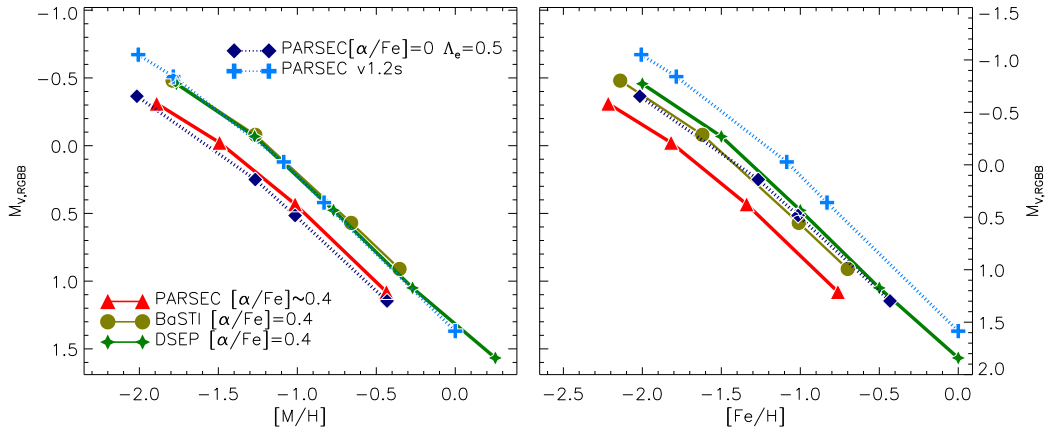


Figure 10. Comparison of the RGBB magnitude of different evolutionary tracks at 13Gyr as a function of $[M/H]$ (left panel) and $[Fe/H]$ (right panel). There are three different α -enhanced models ($[\alpha/Fe]=0.4$) in the figure: PARSEC (red solid line with triangle), BaSTI (yellow green solid line with dot), and DSEP model (green solid line with star). Other two sets of solar-scaled PARSEC models ($[\alpha/Fe]=0$) are plotted for comparison: PARSEC v1.2S with negligible overshoot (light blue dotted line with cross) and PARSEC with EOV calibration $\Lambda_e = 0.5H_p$ (dark blue dotted line with diamond). The Y axis is the mean value of the absolute F606W magnitude of the RGBB ($M_{V,RGBB}$).

parameter lead to a brighter RGBB (Fu 2006). This can explain why in the left panel of Fig. 10 the solar scaled PARSEC v1.2S shows nearly the same $M_{V,RGBB}$ independent of $[M/H]$ as BaSTI and DSEP models. PARSEC v1.2S has slightly higher He content and smaller mixing length parameter which make the RGBB brighter as already discussed above, while its solar scaled metal mixture leads to a fainter RGBB at the same metallicity. The combined effects make the three models to show similar RGBB magnitude. BaSTI and DSEP RGBB have almost the same performance and are eventually brighter than PARSEC $[\alpha/Fe]\sim 0.4$ models no matter as a function of $[M/H]$ or $[Fe/H]$. We remind that a fainter RGBB magnitude can be produced by a more efficient EOV, our new α -enhanced models are computed with the calibrated EOV parameter while, BaSTI and DSEP do not consider envelope overshooting. Also, compared to PARSEC v1.2S ($\Lambda_e = 0.05H_p$) the new solar scaled model with $\Lambda_e = 0.5H_p$ shifts $M_{V,RGBB}$ down by about 0.35 mag. This brightness change is consistent with the work of Cassisi, Salaris & Bono (2002) who conclude that the difference should be of about 0.8 mag/ H_p . Since the RGBB brightness difference between the new PARSEC α -enhanced models and the solar scaled models with the same Λ_e is much smaller than the difference between the two solar scaled PARSEC models with different Λ_e , we conclude that the mixing efficiency has much stronger impact on the RGBB performance than the metal partition.

4.2 Comparison with other GC data

Comparing the location of the RGB bump predicted by the models with the observed one in GCs with different metallicity is a good way to test the models.

In Fig. 11 we compare our new α -enhanced models with HST data from Nataf et al. (2013, 55 clusters) and Cassisi et al. (2011, 12 clusters). The models extend till $[M/H]\sim -2$ ($[Fe/H]\sim -2.3$). For comparison, two sets of models with solar-scaled metal partition, $[\alpha/Fe]=0$ (PARSEC v1.2S and PARSEC with $\Lambda_e = 0.5H_p$) are also plotted.

Here we use the magnitude difference between the RGBB and the main sequence turn-off (MSTO), ΔV_{RGBB}^{MSTO} , as a refer-

ence for comparison between the theoretical magnitude of RGBB and the observed one. Unlike the absolute magnitude $M_{V,RGBB}$, ΔV_{RGBB}^{MSTO} is not affected by uncertainties in the distance modulus $(m-M)_0$ and extinction A_V of the cluster. There are also works using the magnitude difference between HB and RGBB ($\Delta V_{HB}^{RGBB} = M_{V,RGBB} - M_{V,HB}$, e.g. Fusi Pecci et al. 1990; Cassisi & Salaris 1997; Cecco et al. 2010) or the one between HB and MSTO ($\Delta V_{TO}^{HB} = M_{V,TO} - M_{V,HB}$, e.g. Vandenberg et al. 2013) as a way to avoid distance and extinction uncertainties, but, as we have elaborated in Sec. 3.2.4, the RGB mass loss together with different metal mixture and He content may affect the HB magnitude and thus make ΔV_{HB}^{RGBB} difficult to be interpreted. The only free parameter of the ΔV_{RGBB}^{MSTO} method is the age, if the composition of the cluster is fixed. In Fig. 11 we compare the theoretical ΔV_{RGBB}^{MSTO} value at typical GC ages of 11 Gyr and 13 Gyr, with the observed value from Nataf et al. (2013) and (Cassisi et al. 2011). The comparisons are displayed both in the $[M/H]$ frame and $[Fe/H]$ frame. The MSTO in Nataf et al. (2013) is defined by taking the bluest point of a polynomial fit to the upper main sequence of each GC in the (F606W, F606W-F814W). (Cassisi et al. 2011) derive the MSTO magnitude by fitting isochrones to the main sequence. To obtain the theoretical MSTO F606W magnitude in our model, we select the bluest point of the isochrone in the main sequence. The models of 13 Gyr show larger difference between RGBB and MSTO ΔV_{RGBB}^{MSTO} than those at 11 Gyr. Models with $[\alpha/Fe]\sim 0.2$ show a slightly greater ΔV_{RGBB}^{MSTO} value than the models computed with $[\alpha/Fe]\sim 0.4$. In the right panel of the figure we see that the α -enhanced models show greater ΔV_{RGBB}^{MSTO} than the solar scaled ones with the same $[Fe/H]$. This said, if one has $[Fe/H]$ measurement of a GC with α enhancement and takes ΔV_{RGBB}^{MSTO} as an age indicator, choosing the solar scaled models will lead to an underestimated cluster age.

Compared to the previous PARSEC version v1.2S, the new models significantly improve the ΔV_{RGBB}^{MSTO} prediction in both the $[M/H]$ frame and $[Fe/H]$ frame. At the most metal-poor side, around $[M/H]\sim -2.0$ ($[Fe/H]\sim -2.3$), the new models are consistent with Cassisi et al. (2011) data (black dots), but are higher than the values derived by Nataf et al. (2013) (grey dots) by ~ 0.1 mag. We will discuss the possible reasons in the next section.

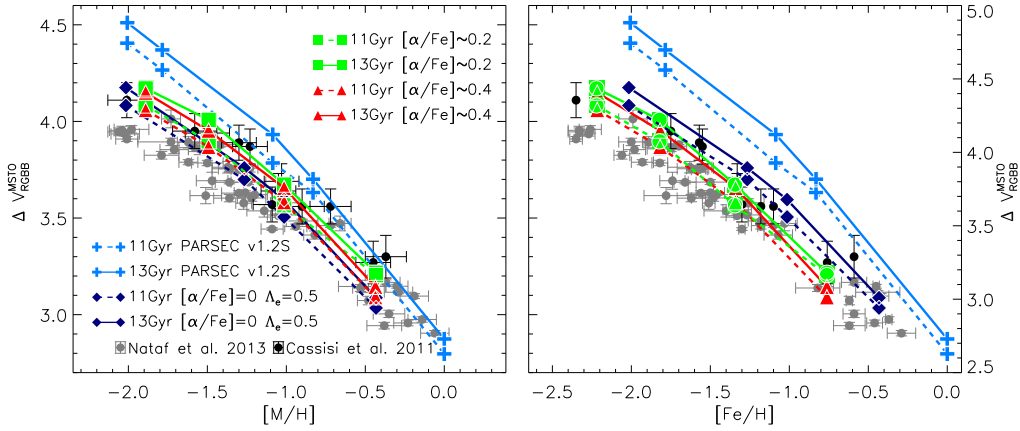


Figure 11. F606W magnitude difference between the MSTO and the RGBB (ΔV_{RGB}^{MSTO}) as a function of the total metallicity [M/H] (left panel) and iron abundance [Fe/H]. Four different sets of theoretical ΔV_{RGB}^{MSTO} value are plotted, at both 13Gyr (solid line) and 11Gyr (dashed line). Three of them are with new calibrated EOV $\Lambda_e = 0.5H_p$: $[\alpha/Fe] \sim 0.4$ (red lines with triangle), $[\alpha/Fe] \sim 0.2$ (green lines with square), and $[\alpha/Fe] = 0$ (dark blue lines with diamond). Another one is from the standard PARSEC v1.2S (light blue lines with cross). The data are 55 clusters from [Nataf et al. \(2013\)](#), grey dots with error bar) and 12 clusters from [Cassisi et al. \(2011\)](#), black dots with error bar).

5 SUMMARY AND DISCUSSION

Studies on globular clusters, Galactic bulge, halo, and thick disk call for stellar models with α enhancement because stars residing in them have α -to-iron number ratio larger than the solar value. This ratio, $[\alpha/Fe]$, not only affects the stellar features like the luminosities and effective temperature, but also echoes the formation history of the cluster/structure the stars are in. To investigate such stars, and to trace back their formation history, we have now extend the PARSEC models to include α -enhanced mixtures.

In this paper we check the α -enhanced models with the nearby globular cluster 47 Tuc (NGC 104). The chemical compositions including the helium abundances of 47 Tuc are studied by many works. We collect detailed elemental abundances of this cluster and derive absolute metal mixtures for two populations: first generation $[Z=0.0056, Y=0.256]$, and second generation $[Z=0.0055, Y=0.276]$. The α -to-iron ratio of them are $[\alpha/Fe] = 0.4057$ ($[\alpha/Fe] \sim 0.4$) and $[\alpha/Fe] = 0.2277$ ($[\alpha/Fe] \sim 0.2$), respectively. We calculate evolutionary tracks and isochrones with these two α -enhanced metal mixtures, and fit color-magnitude diagram to HST/ACS data. The model envelope overshooting is then calibrated to the value $\Lambda_e = 0.5H_p$ in order to reproduce the RGB bump morphology in 47 Tuc. After the calibration, the new α -enhanced isochrones nicely fit the data from the low main sequence to the turn-off, giant branch, and the horizontal branch with age of 12.00 Gyr, distance modulus $(m-M)_0 = 13.22$ ($(m-M)_{F606W} = 13.32$), and reddening $E(6-8) = 0.035$. These results compare favorably with many other determinations in the literature. The luminosity functions inform us that the lifetime of hydrogen burning shell appears to be correctly predicted. By studying the morphology of the horizontal branch, we conclude that the mean mass lost by stars during the RGB phase is around $0.17 M_\odot$.

There are also other methods to estimate the age of this cluster in the literature. For instance, mass-radius constraints of the detached eclipsing binary stars V69 in 47 Tuc have also been used ([Weldrake et al. 2004](#); [Dotter, Kaluzny & Thompson 2008](#); [Thompson et al. 2010](#); [Brogaard et al. 2017](#)). This approach, which considers the two components of the detached binary as single stars, is much less affected by the uncertainties arising from the

unknown distance, reddening and transformation from the theoretical to the observational plane. [Thompson et al. \(2010\)](#) derive an age of 11.25 ± 0.21 (random) ± 0.85 (systematic) for 47 Tuc, and [Brogaard et al. \(2017\)](#) give 11.8 Gyr as their best estimate with 3σ limits from 10.4 Gyr to 13.4 Gyr. We examined the mass-radius and mass-Teff constraints provided by V69 with our best fit FG and SG models at 12.0 Gyr, as shown in Fig. 12. We have adopted for the two components of V69 the following data ([Thompson et al. 2010](#)): current mass $M_p = 0.8762 \pm 0.0048 M_\odot$, $M_s = 0.8588 \pm 0.0060 M_\odot$, radius $R_p = 1.3148 \pm 0.0051 R_\odot$, $R_s = 1.1616 \pm 0.0062 R_\odot$ and effective temperature $T_{eff,p} = 5945 \pm 150$ K, $T_{eff,s} = 5959 \pm 150$ K of the primary and secondary star, respectively. Differences between the FG and SG isochrones are due to the difference of He abundances and $[\alpha/Fe]$. The comparison with our models indicate that V69 cannot belong to the SG population. Concerning the mass-radius relation, which provides the most stringent constraints on the two stars, we see that our best fit FG isochrone of 12 Gyr is only marginally able to reproduce the secondary component (filled black star), within 3σ , while there is a tension with the radius of the primary component (empty star). A better match can be obtained for both components by considering a slightly higher metallicity, as also suggested by [Brogaard et al. \(2017\)](#). For example, the green dashed isochrones in Fig. 12 illustrate the effects of assuming $[Fe/H] = -0.6$ and $[\alpha/Fe] = 0.4$, that correspond to $Z = 0.008$, and an He content of $Y = 0.263$. In this example the He content of the isochrone follows Equ. 1 and the $[\alpha/Fe]$ value is chosen to be 0.4 without any special consideration. We also note that, to bring the radius discrepancy of the primary component within 3σ or 1σ , with the abundances assumed for the FG population, an age of 11.7 Gyr or 11.2 Gyr would be required, respectively. These ages, in particularly the lower one, would be quite different from the one obtained by the best fit presented in the paper. Up to now we have assumed that effects of binary interaction are negligible so that V69 can be analysed with single star evolution models. However considering other possible causes for the discrepancy, we note that the primary component of V69 is among the bluest stars past the turn-off of the CMD (see Fig. 4 of [Thompson et al. 2010](#)) so that the fitting isochrone would likely fit the bluer envelope of the cluster CMD.

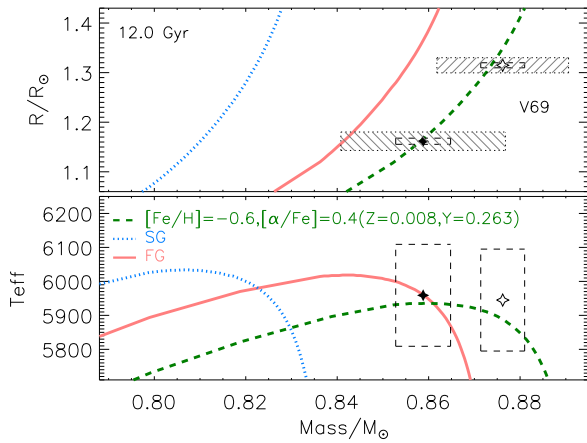


Figure 12. Mass-radius and Mass-Teff diagrams for binary V69. The observed values of the two components of V69 are marked with black stars, their corresponding 1σ and 3σ uncertainties are indicated with dashed line boxes and shaded boxes, respectively (data from [Thompson et al. 2010](#)). Isochrones of 47 Tuc FG (red solid lines) and SG (blue dotted lines) are overlaid. To illustrate the effects of a higher metallicity, isochrones of $[\text{Fe}/\text{H}]=-0.6$, $[\alpha/\text{Fe}]=0.4$ ($Z=0.008$, $Y=0.263$) are also displayed (green dashed lines). All isochrones are with our best estimate age 12.0 Gyr.

We thus suspect that its position in the CMD could partly be due to the effects of the binary dynamical interaction with the companion star. In fact, tidal effects in close binary stars may change the structure and evolution of stars even before any possible mass transfer ([de Mink et al. 2009](#); [Song et al. 2016](#)). In particular, the primary star of V69 matches our model that shows a thin surface convective envelope ($\sim 2\%$ of of total mass) and, following the simple approximation of [Zahn \(1977, equation 6.1\)](#), its tidal synchronization time should be roughly ~ 7.2 Gyr, comparable to its current age. Tidal friction during the previous evolution may have introduced shear mixing and extra turbulence ([Lanza & Mathis 2016](#)) at the base of the external convective region, whose effects are primarily those of mitigating Helium and heavy element diffusion away from the convective region. The net effect will be a lower growth of the surface hydrogen abundance with a corresponding decrease of the current surface opacity, that should result in a smaller current radius, in the observed direction. Of course a more sophisticated theoretical analysis is necessary to assess if the location of the primary star of V69 in the CMD might be affected by previous dynamical interaction, but this is beyond the scope of this paper.

The envelope overshooting calibration together with the α -enhanced metal mixtures of 47 Tuc are applied to other metallicities till $Z=0.0001$. The RGB bump magnitudes of the new α -enhanced isochrones are compared with other stellar models and globular cluster observations. We take $\Delta_{\text{RGBB}}^{\text{MSTO}}$, the magnitude difference between the main sequence turn-off and the RGB bump, as the reference to compare with the observation in order to avoid uncertainties from distance and extinction. Our new models fit the data quite well and significantly improve the prediction of RGB bump magnitude compared to previous models.

However we notice that in Fig. 11 around $[\text{M}/\text{H}]=-2.0$ ($[\text{Fe}/\text{H}]\sim -2.3$) our model predicts $\Delta_{\text{RGBB}}^{\text{MSTO}}$ about ~ 0.1 mag greater than the data points obtained by [Nataf et al. \(2013\)](#). If we consider a more He-rich model with the same metallicity Z , the discrepancy will become even larger. There are works arguing that diffusion also affects the brightness of

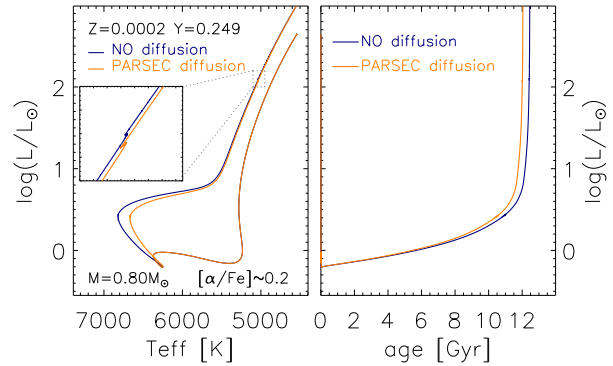


Figure 13. Comparison of $[Z=0.0002 Y=0.249]$ tracks for a $M=0.80 M_{\odot}$ star with (orange line) and without (blue line) diffusion. The left panel shows the HRD of these two tracks, with the RGBB region zoomed in in the sub-figure. The right panel illustrates the luminosity evolution as the star ages.

RGBB (eg. [Michaud, Richer & Richard 2010](#); [Cassisi et al. 2011](#); [Joyce & Chaboyer 2015](#)). [Michaud, Richer & Richard \(2010\)](#) conclude that without atomic diffusion the RGBB luminosity is about 0.02 dex brighter (~ 0.05 mag). In PARSEC we always take diffusion into account. To see the effect of diffusion on RGBB morphology, we calculate a $0.80 M_{\odot}$ model without diffusion and compare it with the one with standard PARSEC diffusion in Fig. 13. The two stars have the same metallicity, He content, stellar mass, and $[\alpha/\text{Fe}]$. As we can see from the right panel diffusion shorten the main sequence life-time. The left panel of this figure is HRD, similar to that in Figure 1 of [Michaud, Richer & Richard \(2010\)](#), evolutionary track with diffusion shows redder MSTO and slightly fainter RGBB. For isochrones obtained from these two sets of evolutionary tracks, at 13 Gyr the RGBB without diffusion is 0.072 mag (in F606W) brighter than the one with diffusion, and $\Delta_{\text{RGBB}}^{\text{MSTO}}$ value is 0.008 mag (in F606W) larger. This result confirms that inhibiting the diffusion during H-burning phase will eventually makes the discrepancy more severe. [Pietrinferni, Cassisi & Salaris \(2010\)](#) conclude that the updated nuclear reaction rate for $^{14}\text{N}(p, \gamma)^{15}\text{O}$ makes RGBB brighter by ~ 0.06 mag compared to the old rate. However we remind that we are already adopting the new rate ([Imbriani et al. 2005](#)) for this reaction (Table 1). Assuming that all other input physics, in particular opacities, is correct, the only possible solution to cover this ~ 0.1 mag discrepancy is that the mixing at the bottom of the convective envelope is even higher than that assumed here. Either EOV in metal-poor stars is larger than our adopted value (e.g $\Lambda_e = 0.7H_p$ suggested by [Alongi et al. 1991](#)) or another kind of extra mixing is responsible.

We have shown in Sec. 4.2 that, comparing the absolute magnitude $M_{\text{V,RGBB}}$ between model and observation directly, would introduce uncertainties from distance and extinction. However putting the $M_{\text{V,RGBB}}$ and $\Delta_{\text{RGBB}}^{\text{MSTO}}$ comparison together, could help us to constrain the distance of the clusters. Fig. 14 displays the differences between the theoretical $M_{\text{V,RGBB}}$ and those of data from [Nataf et al. \(2013\)](#) and [Cassisi et al. \(2011\)](#). The absolute magnitude $M_{\text{V,RGBB}}$ of the data takes into account the apparent distance modulus, hence extinction effects are excluded. The four sets of models in Fig. 14 are the same as those in Fig. 11. The discrepancy of $M_{\text{V,RGBB}}$ between models and the data at the metal-poor end in Fig. 14 is larger than that of $\Delta_{\text{RGBB}}^{\text{MSTO}}$ in Fig. 11 in both $[\text{M}/\text{H}]$ and $[\text{Fe}/\text{H}]$ frames. Since $\Delta_{\text{RGBB}}^{\text{MSTO}}$ is a reference without distance effect,

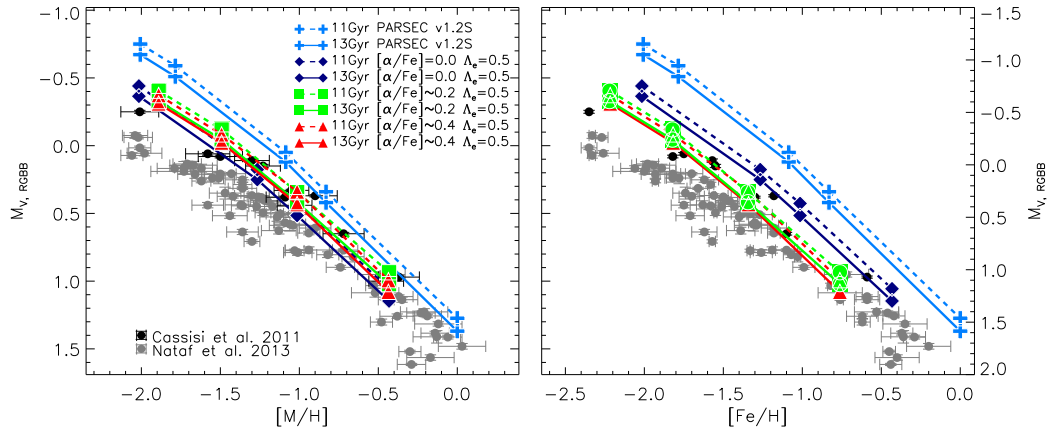


Figure 14. Absolute magnitude in F606W band of RGBB ($M_{V,RGBB}$) as a function of metallicity [M/H] (left panel) and iron abundance [Fe/H] (right panel). Three sets of EOV-calibrated PARSEC models, $[\alpha/Fe]=[0.0, 0.2, 0.4]$, and PARSEC v1.2S are shown both at age 13Gyr (solid line) and 11Gyr (dashed line). For comparison, Nataf et al. (2013, grey filled dots with error bar) and Cassisi et al. (2011, black filled dots with error bar) RGBB data are plotted. See the text for the details.

this larger discrepancy indicates that the apparent distance modulus $(m-M)_V$ used in Fig. 14 (Nataf et al. 2013) for metal-poor GCs are underestimated.

In a following paper of the “PARSEC α -enhanced stellar evolutionary tracks and isochrones” series, we will provide other $[\alpha/Fe]$ choices based on metal mixtures derived from ATLAS9 APOGEE atmosphere models (Mészáros et al. 2012). The full set of isochrones with chemical compositions suitable for GCs and Galactic bulge/thick disk stars will be available online after the full calculation and calibration are performed.

6 ACKNOWLEDGEMENTS

XF thanks Angela Bragaglia and Francesca Primas for the useful discussion, and Fiorella Castelli for the guide on ATLAS12 calculation. AB acknowledges PRIN INAF 2014 ‘Star formation and evolution in galactic nuclei’, and thanks Michela Mapelli for the useful discussion on binary interaction. PM, JM, YC and AN acknowledge support from the ERC Consolidator Grant funding scheme (project STARKEY, G. A. n. 615604).

REFERENCES

- Alongi M., Bertelli G., Bressan a., Chiosi C., 1991, *A&A*, 244, 95
 Alves-Brito A. et al., 2005, *A&A*, 667, 657
 Anderson J., Piotto G., King I. R., Bedin L. R., Guhathakurta P., 2009, *ApJ*, 697, L58
 Anderson J. et al., 2008, *AJ*, 135, 2055
 Angulo C. et al., 1999, *Nucl. Phys. A*, 656, 3
 Balbinot E. et al., 2016, *ApJ*, 820, 58
 Bedin L. R., Piotto G., Anderson J., Cassisi S., King I. R., Momany Y., Carraro G., 2004, *ApJ*, 605, L125
 Belczynski K., Holz D. E., Bulik T., O’Shaughnessy R., 2016, *Nature*, 534, 512
 Bergbusch P. A., Stetson P. B., 2009, *AJ*, 138, 1455
 Betts R. R., Fortune H. T., Middleton R., 1975, *Phys. Rev. C*, 11, 19
 Bjork S. R., Chaboyer B., 2006, *ApJ*, 641, 1102
 Bono G., Cassisi S., Zoccali M., Piotto G., 2001, *ApJ*, 546, L109
 Borissova J. et al., 2014, *A&A*, 569, A24
 Bovy J., Rix H.-W., Green G. M., Schlafly E. F., Finkbeiner D. P., 2016, *ApJ*, 818, 130
 Bragaglia A., Carretta E., Gratton R., D’Orazi V., Cassisi S., Lucatello S., 2010, *A&A*, 519, A60
 Bragaglia A., Carretta E., Sollima A., Donati P., D’Orazi V., Gratton R. G., Lucatello S., Sneden C., 2015, *A&A*, 583, A69
 Bressan A., Girardi L., Marigo P., Rosenfield P., Tang J., 2015, in *Astrophysics and Space Science Proceedings*, Vol. 39, *Asteroseismology of Stellar Populations in the Milky Way*, Miglio A., Eggenberger P., Girardi L., Montalbán J., eds., p. 25
 Bressan A., Marigo P., Girardi L., Salasnich B., Dal Cero C., Rubele S., Nanni A., 2012, *MNRAS*, 427, 127
 Briley M. M., 1997, *AJ*, 114, 1051
 Brogaard K., Vandenberg D. A., Bedin L. R., Milone A. P., Thygesen A., Grundahl F., 2017, *MNRAS*, 468, 645
 Caffau E., Ludwig H.-G., Steffen M., Freytag B., Bonifacio P., 2011, *Sol. Phys.*, 268, 255
 Caloi V., D’Antona F., 2005, *A&A*, 435, 987
 Cannon R. D., Croke B. F. W., Bell R. A., Hesser J. E., Stathakis R. A., 1998, *MNRAS*, 298, 601
 Cardelli J. A., Clayton G. C., Mathis J. S., 1989, *ApJ*, 345, 245
 Carney B. W., 1996, *Publications of the Astronomical Society of the Pacific*, 108, 900
 Carretta E., Bragaglia A., Gratton R., D’Orazi V., Lucatello S., 2009a, *A&A*, 508, 695
 Carretta E., Bragaglia A., Gratton R., Lucatello S., 2009b, *A&A*, 505, 139
 Carretta E., Bragaglia A., Gratton R. G., Leone F., Recio-Blanco A., Lucatello S., 2006, *A&A*, 450, 523
 Carretta E. et al., 2007, *A&A*, 464, 967
 Carretta E., D’Orazi V., Gratton R. G., Lucatello S., 2014, *A&A*, 563, A32
 Carretta E., Gratton R. G., Bragaglia A., D’Orazi V., Lucatello S., 2013, *A&A*, 550, A34
 Casey A. R. et al., 2016, *MNRAS*, 461, 3336
 Cassisi S., Marin-Franch A., Salaris M., Aparicio A., Monelli M., Pietrinfermi A., 2011, *A&A*, 527, A59

- Cassisi S., Salaris M., 1997, *MNRAS*, 285, 593
- Cassisi S., Salaris M., Bono G., 2002, *ApJ*, 565, 1231
- Catelan M., 2008, *Proceedings of the International Astronomical Union*, 4, 209
- Caughlan G. R., Fowler W. A., 1988, *Atomic Data and Nuclear Data Tables*, 40, 283
- Cecco A. D. et al., 2010, *ApJ*, 712, 527
- Chen Y., Bressan A., Girardi L., Marigo P., Kong X., Lanza A., 2015, *MNRAS*, 452, 1068
- Chen Y., Girardi L., Bressan A., Marigo P., Barbieri M., Kong X., 2014, *MNRAS*, 444, 2525
- Chevallard J., Charlot S., 2016, *MNRAS*, 462, 1415
- Chiosi C., Bressan A., Portinari L., Tantalo R., 1998, *A&A*, 381, 355
- Choi J., Dotter A., Conroy C., Cantiello M., Paxton B., Johnson B. D., 2016, *ApJ*, 823, 102
- Christensen-Dalsgaard J., Monteiro M. J. P. F. G., Rempel M., Thompson M. J., 2011, *MNRAS*, 414, 1158
- Constantini H., LUNA Collaboration, 2010, in *Nuclei in the Cosmos*, p. 14
- Cordero M. J., Pilachowski C. a., Johnson C. I., McDonald I., Zijlstra a. a., Simmerer J., 2014, *ApJ*, 780, 94
- Cybur R. H., 2012, Re-evaluation of Buchmann 1996 C12(a,g) and Hoffman Ca40(a,g) and Ti44(a,p) rates. REACLIB
- Cybur R. H. et al., 2010, *ApJS*, 189, 240
- Cybur R. H., Davids B., 2008, *Phys. Rev. C*, 78, 064614
- D'Antona F., Bellazzini M., Caloi V., Pecci F. F., Galletti S., Rood R. T., 2005, *ApJ*, 631, 868
- D'Antona F., Caloi V., Montalbán J., Ventura P., Gratton R., 2002, *A&A*, 395, 69
- de Mink S. E., Cantiello M., Langer N., Pols O. R., Brott I., Yoon S.-C., 2009, *A&A*, 497, 243
- Descouvemont P., Adahchour A., Angulo C., Coc A., Vangioni-Flam E., 2004, *Atomic Data and Nuclear Data Tables*, 88, 203
- Di Criscienzo M., Ventura P., D'Antona F., Milone a., Piotto G., 2010, *MNRAS*, 408, 999
- Dobrovolskas V. et al., 2014, *A&A*, 565, A121
- Donati P. et al., 2014, *A&A*, 561, A94
- D'Orazi V., Lucatello S., Gratton R., Bragaglia A., Carretta E., Shen Z., Zaggia S., 2010, *ApJ*, 713, L1
- Dotter A., Chaboyer B., Jevremović D., Baron E., Ferguson J. W., Sarajedini A., Anderson J., 2007, *AJ*, 134, 376
- Dotter A., Chaboyer B., Jevremović D., Kostov V., Baron E., Ferguson J. W., 2008, *ApJS*, 178, 89
- Dotter A., Kaluzny J., Thompson I. B., 2008, *Proceedings of the International Astronomical Union*, 4, 171176
- Dotter A. et al., 2010, *ApJ*, 708, 698
- Dotter A. L., 2007, PhD thesis, Dartmouth College
- Dupree A. K., Strader J., Smith G. H., 2011, *ApJ*, 728, 155
- Fagotto F., Bressan A., Bertelli G., Chiosi C., 1994, *A&AS*, 104
- Fu X., 2006, PhD thesis, SISSA - International School for Advanced Studies, Via Bonomea 265, 34136 Trieste, Italy
- Fu X., Bressan A., Molaro P., Marigo P., 2015, *MNRAS*, 452, 3256
- Fulbright J. P., 2002, *AJ*, 123, 404
- Fusi Pecci F., Bellazzini M., 1997, in *The Third Conference on Faint Blue Stars*, Philip A. G. D., Liebert J., Saffer R., Hayes D. S., eds., p. 255
- Fusi Pecci F., Ferraro F. R., Crocker D. A., Rood R. T., Buonanno R., 1990, *A&A*, 238, 95
- Fynbo H. O. U. et al., 2005, *Nature*, 433, 136
- Gonzalez O. A. et al., 2011, *A&A*, 530, A54
- Goudfrooij P., Girardi L., Rosenfield P., Bressan A., Marigo P., Correnti M., Puzia T. H., 2015, *MNRAS*, 450, 1693
- Gratton R. G. et al., 2001, *A&A*, 369, 87
- Gratton R. G., Carretta E., Bragaglia A., 2012, *A&A Rev.*, 20, 50
- Gratton R. G., Carretta E., Bragaglia A., Lucatello S., D'Orazi V., 2010, *A&A*, 517, A81
- Gratton R. G. et al., 2013, *A&A*, 549, A41
- Gratton R. G. et al., 2015, *A&A*, 573, A92
- Gullikson K., Kraus A., Dodson-Robinson S., 2016, *AJ*, 152, 40
- Gutkin J., Charlot S., Bruzual G., 2016, *MNRAS*, 462, 1757
- Hansen B. M. S. et al., 2013, *Nature*, 500, 51
- Harbeck D., Smith G. H., Grebel E. K., 2003, *AJ*, 125, 197
- Harris W. E., 1996, *AJ*, 112, 1487
- Heil M. et al., 2008, *Phys. Rev. C*, 78, 025803
- Herwig F., 2000, *A&A*, 360, 952
- Heyl J., Kalirai J., Richer H. B., Marigo P., Antolini E., Goldsbury R., Parada J., 2015, *ApJ*, 810, 127
- Iglesias C. A., Rogers F. J., 1996, *ApJ*, 464, 943
- Iliadis C., Angulo C., Descouvemont P., Lugaro M., Mohr P., 2008, *Phys. Rev. C*, 77, 045802
- Iliadis C., Longland R., Champagne A. E., Coc A., 2010, *Nuclear Physics A*, 841, 251
- Imbriani G. et al., 2005, *European Physical Journal A*, 25, 455
- Itoh N., Uchida S., Sakamoto Y., Kohyama Y., Nozawa S., 2008, *ApJ*, 677, 495
- Johnson C. I., Rich R. M., Kobayashi C., Kunder A., Koch A., 2014, *AJ*, 148, 67
- Joyce M., Chaboyer B., 2015, *ApJ*, 814, 142
- Kalari V. M. et al., 2014, *A&A*, 564, L7
- Kalirai J. S. et al., 2012, *AJ*, 143, 11
- Kim Y., Demarque P., Yi S. K., Alexander D. R., 2002, *ApJS*, 143, 499
- King C. R., Da Costa G. S., Demarque P., 1985, *ApJ*, 299, 674
- Kirby E. N., Cohen J. G., Smith G. H., Majewski S. R., Sohn S. T., Guhathakurta P., 2011, *ApJ*, 727, 79
- Komatsu E. et al., 2011, *ApJS*, 192, 18
- Küpper A. H. W., Balbinot E., Bonaca A., Johnston K. V., Hogg D. W., Kroupa P., Santiago B. X., 2015, *ApJ*, 803, 80
- Kurucz R. L., 2005, *Memorie della Societa Astronomica Italiana Supplementi*, 8, 14
- Lanza A. F., Mathis S., 2016, *Celestial Mechanics and Dynamical Astronomy*, 126, 249
- Lebreton Y., Goupil M. J., 2012, *A&A*, 544, L13
- Li J. et al., 2016, *ApJ*, 823, 59
- Li Z. et al., 2010, *Science China Physics, Mechanics, and Astronomy*, 53, 658
- Maldonado J., Eiroa C., Villaver E., Montesinos B., Mora A., 2015, *A&A*, 579, A20
- Marigo P., Aringer B., 2009, *A&A*, 508, 1539
- Marigo P., Bressan A., Nanni A., Girardi L., Pumo M. L., 2013, *MNRAS*, 434, 488
- Marigo P., Girardi L., 2007, *A&A*, 469, 239
- Marigo P. et al., 2017, *ApJ*, 835, 77
- Marino A. F. et al., 2014, *MNRAS*, 437, 1609
- Marino A. F. et al., 2011, *A&A*, 532, A8
- McDonald I., Zijlstra A. A., 2015, *MNRAS*, 448, 502
- McWilliam A., Preston G. W., Sneden C., Searle L., 1995, *AJ*, 109, 2757
- Mészáros S. et al., 2012, *AJ*, 144, 120
- Michaud G., Richer J., Richard O., 2010, *A&A*, 510, A104
- Milone A. P. et al., 2008, *ApJ*, 673, 241
- , 2015a, *MNRAS*, 450, 3750

- Milone A. P., Marino A. F., D'Antona F., Bedin L. R., Da Costa G. S., Jerjen H., Mackey A. D., 2016, *MNRAS*, 458, 4368
- Milone A. P., Marino A. F., Piotto G., Bedin L. R., Anderson J., Aparicio A., Cassisi S., Rich R. M., 2012, *ApJ*, 745, 27
- Milone A. P. et al., 2015b, *ApJ*, 808, 51
- Milone A. P. et al., 2012, *ApJ*, 744, 58
- Milone A. P. et al., 2010, *ApJ*, 709, 1183
- Mucciarelli A., Lovisi L., Lanzoni B., Ferraro F. R., 2014, *ApJ*, 786, 14
- Nanni A., Bressan A., Marigo P., Girardi L., 2013, *MNRAS*, 434, 2390
- Nanni A., Bressan A., Marigo P., Girardi L., 2014, *MNRAS*, 438, 2328
- Nataf D. M., Gould A., Pinsonneault M. H., Stetson P. B., 2011, *ApJ*, 736, 94
- Nataf D. M., Gould A. P., Pinsonneault M. H., Udalski A., 2013, *ApJ*, 766, 77
- Nataf D. M., Udalski A., Gould A., Pinsonneault M. H., 2011, *ApJ*, 730, 118
- Nissen P. E., Gustafsson B., Edvardsson B., Gilmore G., 1994, *A&A*, 285, 440
- Norris J., Freeman K. C., 1979, *ApJ*, 230, L179
- Origlia L., Rood R. T., Fabbri S., Ferraro F. R., Fusi Pecci F., Rich R. M., 2007, *ApJ*, 667, L85
- Pasquini L., Mauas P., Käufel H. U., Cacciari C., 2011, *A&A*, 531, A35
- Perren G. I., Vázquez R. A., Piatti A. E., 2015, *A&A*, 576, A6
- Pietrinferni A., Cassisi S., Salaris M., 2010, *A&A*, 522, A76
- Pietrinferni A., Cassisi S., Salaris M., Castelli F., 2006, *ApJ*, 642, 797
- Pietrinferni A., Cassisi S., Salaris M., Hidalgo S., 2013, *A&A*, 558, A46
- Piotto G. et al., 2007, *ApJ*, 661, L53
- Pritzl B. J., Venn K. a., Irwin M., 2005, *AJ*, 130, 2140
- Ramya P., Reddy B. E., Lambert D. L., Musthafa M. M., 2016, *MNRAS*, 460, 1356
- Reddy A. B. S., Lambert D. L., 2016, *A&A*, 589, A57
- Reddy B. E., Lambert D. L., Prieto C. A., 2006, *MNRAS*, 367, 1329
- Reimers D., 1975, *Memoires of the Societe Royale des Sciences de Liege*, 8, 369
- Rood R. T., Crocker D. A., 1985, in *European Southern Observatory Conference and Workshop Proceedings*, Vol. 21, *European Southern Observatory Conference and Workshop Proceedings*, Danziger I. J., Matteucci F., Kjar K., eds., pp. 61–69
- Rosenfield P., Marigo P., Girardi L., Dalcanton J. J., Bressan A., Williams B. F., Dolphin A., 2016, *ApJ*, 822, 73
- Ruchti G. R. et al., 2010, *ApJ*, 721, L92
- Salaris M., Cassisi S., Pietrinferni A., 2016, *A&A*, 590, A64
- Salaris M., Held E. V., Ortolani S., Gullieuszik M., Momany Y., 2007, *A&A*, 476, 243
- Salaris M., Weiss A., Ferguson J. W., Fusilier D. J., 2006, *ApJ*, 645, 1131
- Salasnich B., Girardi L., Weiss A., Chiosi C., 2000, *A&A*, 361, 1023
- Salpeter E. E., 1955, *ApJ*, 121, 161
- San Roman I. et al., 2015, *A&A*, 579, A6
- Sandage A., Wildey R., 1967, *ApJ*, 150, 469
- Santos N. C. et al., 2013, *A&A*, 556, A150
- Sarajedini A. et al., 2007, *AJ*, 133, 1658
- Schlafly E. F. et al., 2014, *ApJ*, 789, 15
- Schultheis M. et al., 2015, *A&A*, 577, A77
- Smiljanic R. et al., 2016, *A&A*, 589, A115
- Snedden C., 2004, *Mem. Soc. Astron. Italiana*, 75, 267
- Song H. F., Meynet G., Maeder A., Ekström S., Eggenberger P., 2016, *A&A*, 585, A120
- Spada F., Demarque P., Kim Y. C., Sills A., 2013, *ApJ*, 776, 87
- Spera M., Mapelli M., Bressan A., 2015, *MNRAS*, 451, 4086
- Strandberg E. et al., 2008, *Phys. Rev. C*, 77, 055801
- Tang J., Bressan A., Rosenfield P., Slemmer A., Marigo P., Girardi L., Bianchi L., 2014, *MNRAS*, 445, 4287
- Thompson I. B., Kaluzny J., Rucinski S. M., Krzeminski W., Pych W., Dotter A., Burley G. S., 2010, *AJ*, 139, 329
- Thygesen A. O. et al., 2014, *A&A*, 572, A108
- Troisi F. et al., 2011, *Publications of the Astronomical Society of the Pacific*, 123, 879
- Tuli J. K., 2011, *Weak rates from the Nuclear Wallet Cards*. National Nuclear Data Center
- Valcarce A. A. R., Catelan M., Sweigart A. V., 2012, *A&A*, 547, A5
- van den Bergh S., 1967, *AJ*, 72, 70
- VandenBerg D. A., 2013, in *IAU Symposium*, Vol. 289, *Advancing the Physics of Cosmic Distances*, de Grijs R., ed., pp. 161–168
- VandenBerg D. a., Bergbusch P. a., Dotter A., Ferguson J. W., Michaud G., Richer J., Proffitt C. R., 2012, *ApJ*, 755, 15
- VandenBerg D. a., Bergbusch P. a., Ferguson J. W., Edvardsson B., 2014, *ApJ*, 794, 72
- VandenBerg D. a., Brogaard K., Leaman R., Casagrande L., 2013, *ApJ*, 775, 134
- VandenBerg D. A., Swenson F. J., Rogers F. J., Iglesias C. A., Alexander D. R., 2000, *ApJ*, 532, 430
- Venn K. A., Irwin M., Shetrone M. D., Tout C. A., Hill V., Tolstoy E., 2004, *AJ*, 128, 1177
- Villanova S., Piotto G., Gratton R. G., 2009, *A&A*, 499, 755
- Villanova S. et al., 2007, *ApJ*, 663, 296
- Watkins L. L., van der Marel R. P., Bellini A., Anderson J., 2015, *ApJ*, 812, 149
- Weldrake D. T. F., Sackett P. D., Bridges T. J., Freeman K. C., 2004, *AJ*, 128, 736
- Zahn J.-P., 1977, *A&A*, 57, 383
- Zhao G., Magain P., 1990, *A&A*, 238, 242
- Zoccali M., Cassisi S., Piotto G., Bono G., Salaris M., 1999, *ApJ*, 518, L49